33RD CONGRESS
OF THE INTERNATIONAL COUNCIL
OF THE AERONAUTICAL SCIENCES
STOCKHOLM, SWEDEN, 4-9 SEPTEMBER, 2022

ICAS 2022 SWEDEN

FLIGHT CONTROLLABILITY ANALYSIS IN TIGHT FORMATION AND CRUISE FLIGHT FOR FUEL SAVING

Daniel Barbuto Rossato[1] & Karl Heinz Kienitz[2]

[1]Faculdade de Tecnologia SENAI "Mariano Ferraz" - R. Jaguaré Mirim, 71, Vila Leopoldina, São Paulo, Brazil
[2]Instituto Tecnológico de Aeronáutica - Pca. Mal. Eduardo Gomes, 50, Vila das Acacias, São José dos Campos, Brazil

Abstract

Tight formation flight can lead to a significant amount of fuel savings. However, disturbances due to the wake vortex encounter at the wingman impose a limitation on the flight controllability. In this work, the aircraft model including the dynamics and input saturation of control surfaces and engines are considered in an analysis of controllability inside the vortex field in a tight formation flight of two medium-size cargo aircraft. In general, extremum-seeking algorithms are used to seek and maintain the aircraft in the sweet-spot region. Thus, an analysis of the controllability is carried out to this condition as well by means of a trim algorithm.

Keywords: tight formation, flight controllability, efficiency, fuel saving

1. Introduction

Using the same principle of the formation flight of birds to save fuel consumption by an aircraft is not a new idea. Weiselsberger [1] used the lifting line theory recently developed by Prandtl at that time to describe a V formation of three birds where the trailing birds take advantage of the updraft from the vortices of the lead bird. The concept is currently known as $AVE (Surfing Aircraft Vortices for Energy) or AWSE (Air-Wake-Surfing for Efficiency).

Several flight tests with different types of aircraft has demonstrated savings up to 18% in tight formation flight (distance up to 10 wingspans from the leader) [2] [3] [4] [5] and up to 10% in extended formations (distance more than 10 wingspans) [6] [7] [8].

Several models to describe the wake vortex of the leader aircraft were developed [9] [10]. However, an accurate model to describe more precisely the vortex behaviour and the encounter effects over the wingman aircraft for tight formation flight were described in [11].

Since then, the design of a control system for tight formation flight has been proposed [12] [13] [14].

Recently, a Research Task Group (RTG) named AVT-279 from the NATO Science and Technology Organization (STO) has studied the formation flying for efficient operations and has been reporting history, achievements, and roadmap [15].

However, as far as we know these works do not approach the question of the flight controllability inside the vortex in tight formation flight.

Thus, we seek to answer questions such as: what are the limits of controllability of the wingman inside the vortex, in other words, how to measure that the aircraft can be controlled safely while seeking to save energy inside the vortex? Is it possible to fly comfortably i.e., in almost straight and level flight? Is differential throttle helpful in this condition?

For that purpose, in Section 2. the model of the wingman inside the vortex is discussed, and the influence of the disturbance due to the encounter vortex effects is analysed in Section 3. regarding the input saturation. Finally, in Section 4. a trim algorithm is applied for different situations to analyse the flight controllability for each case when the aircraft seeks to save fuel inside the vortex.

Therefore, this work aims to contribute both to the definition of control strategies for the autopilot and the specification of criteria for technical standards of acceptance of formation flight for fuel saving in regular flights.

2. Modeling

The considered scenario is that of two similar cargo aircraft on a cruise flight. Parameters of the model were obtained for the VFW-614-ATTAS aircraft at a straight-level flight at 6,000 m of altitude, a true airspeed of 170 m/s, a weight of 17.4 t and a wingspan of 21.5 m [16]. ATTAS stands for Advanced Technologies Testing Aircraft System. It is a modification for research purposes of the twin-engine VFW-614 short-haul jet developed by Fokker.

The linearised equation of wingman motion is given by [12]:

$$\begin{aligned} \dot{x} &= Ax + Bu + Fd(y_o, z_o) \\ \begin{bmatrix} \dot{x}_t \\ \dot{x}_n \end{bmatrix} &= \begin{bmatrix} A_t & \mathbf{0} \\ \mathbf{0} & A_n \end{bmatrix} \begin{bmatrix} x_t \\ x_n \end{bmatrix} + \begin{bmatrix} B_t & \mathbf{0} \\ \mathbf{0} & B_n \end{bmatrix} \begin{bmatrix} u_t \\ u_n \end{bmatrix} + \begin{bmatrix} F_t & \mathbf{0} \\ \mathbf{0} & F_n \end{bmatrix} \begin{bmatrix} d_t(y_o, z_o) \\ d_n(y_o, z_o) \end{bmatrix} \end{aligned} \tag{1}$$

where the indices t and n refers to the lateral and longitudinal motion (with engines dynamics included) respectively; input variables are: $u_t = \begin{bmatrix} \delta_a & \delta_r \end{bmatrix}^T$ and $u_n = \begin{bmatrix} \delta_e & \delta_{t_{LH}} & \delta_{t_{RH}} \end{bmatrix}^T$, where: δ_a, δ_r and δ_e are the control surfaces aileron, rudder and elevator, and $\delta_{t_{LH}}$ and $\delta_{t_{RH}}$ are the throttle of each engine; state variables of the lateral model are: $x_t = \begin{bmatrix} y_o & v & p & r & \phi & \psi \end{bmatrix}^T$; state variables of the longitudinal model: $x_n = \begin{bmatrix} z_o & x_o & u & w & q & \theta & n_{LH} & \dot{n}_{LH} & ff_{LH} & n_{RH} & \dot{n}_{RH} & ff_{RH} \end{bmatrix}^T$; where x_o, y_o and z_o are the relative coordinates of the wingman regarding the leader aircraft; u, v and w are the linear velocities; p, q and r the angular velocities, all regarding the x, y and z axes of the body coordinate system; ϕ, θ and ψ are the roll, pitch and yaw angles; n, $\dot{n}$ and ff are the engine variables: angular velocity, angular acceleration and fuel flow, LH and RH stands for left-hand side and right-hand side.

All variables are considered as incremental values regarding the trim condition with values in SI units. The trimmed values of the input variables are:

$$\bar{u_t} = \begin{bmatrix} \bar{\delta}_a \\ \bar{\delta}_r \end{bmatrix} = \begin{bmatrix} 0 \\ 0 \end{bmatrix} \tag{2}$$

$$\bar{u_n} = \begin{bmatrix} \bar{\delta}_e \\ \bar{\delta}_{tLH} \\ \bar{\delta}_{tRH} \end{bmatrix} = \begin{bmatrix} 0 \\ 41.09 \\ 41.09 \end{bmatrix} . \tag{3}$$

The terms $d_t(y_o, z_o)$ and $d_n(y_o, z_o)$ are the velocities induced by the wake vortex encounter considered as disturbances: v_g, p_g, r_g (lateral) and u_g,w_g,q_g (longitudinal).

Although the induced velocities can change in time, it will be considered here that they are static as the distance x_o between the leader and the wingman aircraft will be regulated to stay constant.

These values were obtained using a wake vortex encounter (WVE) software package developed in the European S-Wake project and modified to include the model of the wake roll-up in the near field region (from 0 up to 15 wingspans) as presented in [11]. Data of a discrete static field map along the y_o and z_o axes from static simulation of the vortex were kindly provided by André Kaden from TUB, considering the same scenario studied here with a distance x_o of 5 wingspans behind the leading aircraft. Figs. 1,2,3,4,5 show the graphs from the simulation data of these velocities induced by the wake vortex.

Matrices F_t and F_n are defined following the rationale in [17] for lateral and longitudinal models respectively:

$$\begin{aligned} \begin{bmatrix} \dot{v} \\ \dot{p} \\ \dot{r} \\ \dot{\phi} \\ \dot{\psi} \end{bmatrix} &= \begin{bmatrix} Y'_v & Y'_p + w_0 & Y'_r - u_0 & gc_{\theta_0} & 0 \\ L'_v & L'_p & L'_r & 0 & 0 \\ N'_v & N'_p & N'_r & 0 & 0 \\ 0 & 1 & 0 & 0 & 0 \\ 0 & 0 & 1 & 0 & 0 \end{bmatrix} \begin{bmatrix} v \\ p \\ r \\ \phi \\ \psi \end{bmatrix} + \begin{bmatrix} Y'_{\delta_a} & Y'_{\delta_r} \\ L'_{\delta_a} & L'_{\delta_r} \\ N'_{\delta_a} & N'_{\delta_r} \\ 0 & 0 \\ 0 & 0 \end{bmatrix} \begin{bmatrix} \delta_a \\ \delta_r \end{bmatrix} + \\ &\quad \begin{bmatrix} -Y'_v & -Y'_p & -Y'_r \\ -L'_v & -L'_p & -L'_r \\ -N'_v & -N'_p & -N'_r \\ 0 & 0 & 0 \\ 0 & 0 & 0 \end{bmatrix} \begin{bmatrix} v_g \\ p_g \\ r_g \end{bmatrix} \end{aligned} \tag{4}$$

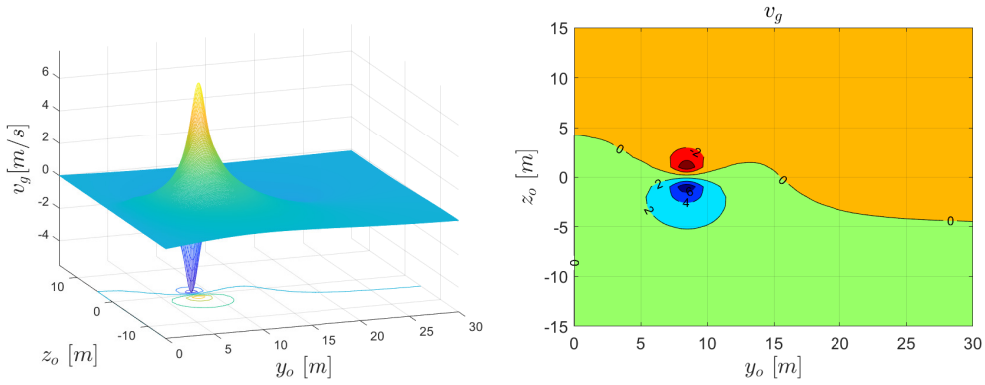

Figure 1 – Vortex Induced Velocities: v_g

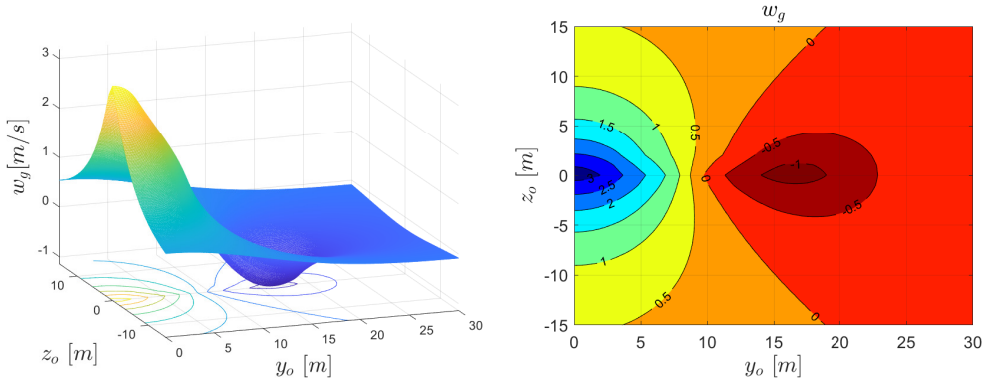

Figure 2 – Vortex Induced Velocities: w_g

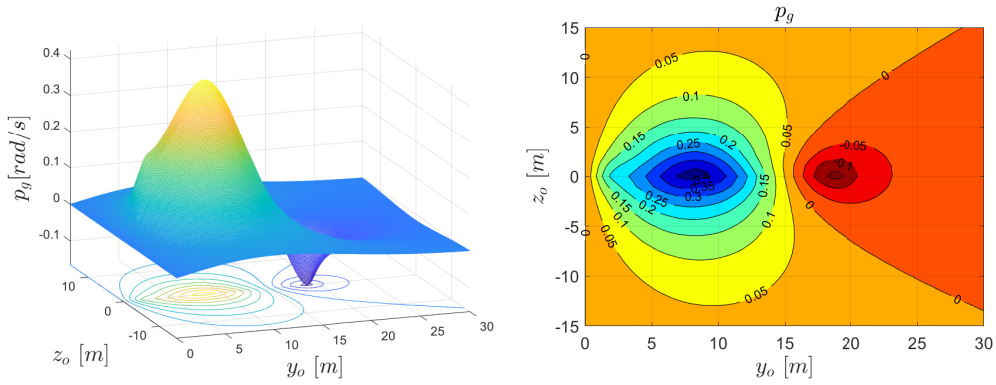

Figure 3 – Vortex Induced Velocities: p_g

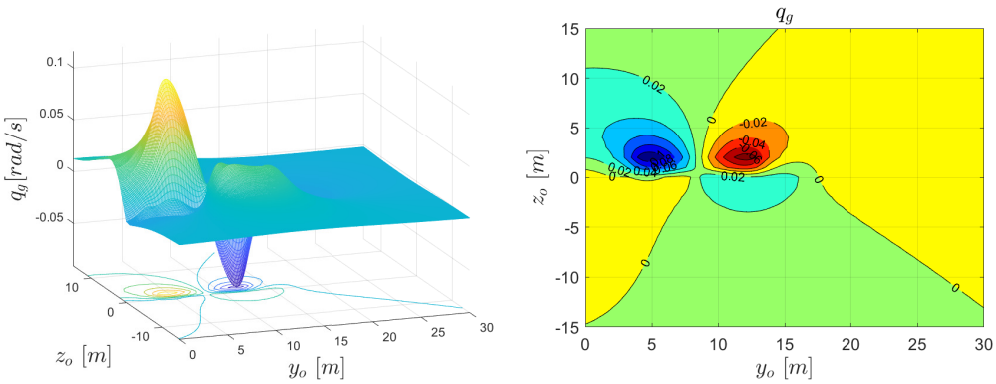

Figure 4 – Vortex Induced Velocities: q_g

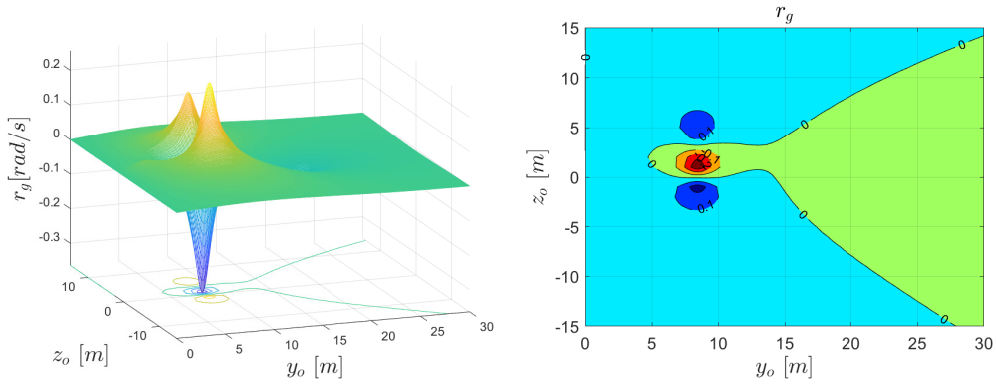

Figure 5 – Vortex Induced Velocities: r_g

$$\begin{bmatrix} \dot{u} \\ \dot{w} \\ \dot{q} \\ \dot{\theta} \end{bmatrix} = \begin{bmatrix} X'_u & X'_w & X'_q - w_0 & -gc_{\theta_0} \\ Z'_u & Z'_w & Z'_q + u_0 & -gs_{\theta_0} \\ M'_u & M'_w & M'_q & 0 \\ 0 & 0 & 1 & 0 \end{bmatrix} \begin{bmatrix} u \\ w \\ q \\ \theta \end{bmatrix} + \begin{bmatrix} X'_{\delta_e} & X'_{\delta_t} \\ Z'_{\delta_e} & Z'_{\delta_t} \\ M'_{\delta_e} & M'_{\delta_t} \\ 0 & 0 \end{bmatrix} \begin{bmatrix} \delta_e \\ \delta_t \end{bmatrix} + \begin{bmatrix} -X'_u & -X'_w & -X'_q \\ -Z'_u & -Z'_w & -Z'_q \\ -M'_u & -M'_w & -M'_q \\ 0 & 0 & 0 \end{bmatrix} \begin{bmatrix} u_g \\ w_g \\ q_g \end{bmatrix} \tag{5}$$

3. Disturbance Analysis

The input-output controllability is a term used to describe the ability of the plant to achieve acceptable control performance, in other words, to keep the output (y) within specific bounds from their references (r), despite unknown but bounded variations (disturbances and uncertainties), using available inputs (u) and available measurements (y_m) [18].

There are some limitations on the system performance due to inherent control characteristics, that should be investigated such as the ability to reject disturbances, presence of time-delays, RHP-zeros, RHP-poles, and uncertainties.

In that Section, the ability of the aircraft to reject disturbances due to the wake vortex influence will be investigated considering the input saturation.

3.1 Disturbance rejection in the lateral motion

Consider the linearised state-space model of the lateral motion in Eq. 1. The scaled closed-loop system for rejecting disturbances is shown in Fig. 6.

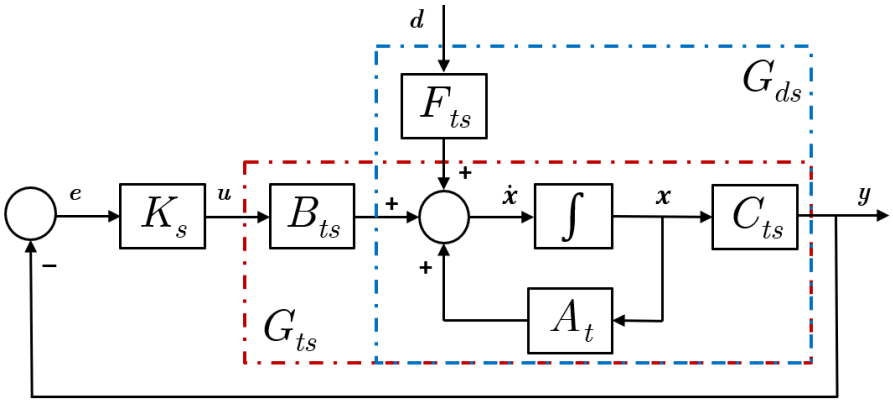

Figure 6 – Diagram block of scaled linear system

In the block diagram, $B_{ts} = B_t D_{ut}$, where D_{ut} is a diagonal matrix with the maximum values of each input signal:

$$D_{ut} = \begin{bmatrix} \delta_{a_{max}} & 0 \\ 0 & \delta_{r_{max}} \end{bmatrix} = \begin{bmatrix} 0.35 & 0 \\ 0 & 0.26 \end{bmatrix}. \tag{6}$$

The block $C_{ts} = D_{yt}^{-1} C_t$, where D_{yt} is a diagonal matrix with the maximum desired values of each output signal: 1 degree (or $\pi/180$ rad) for the angles ϕ, ψ and β (where $\beta = 0.0059v$), 1 rad/s for angular velocities p and r, and 1 m for y_o. Thus,

$$D_{yt} = \begin{bmatrix} y_{o_{max}} & 0 & 0 & 0 & 0 & 0 \\ 0 & v_{max} & 0 & 0 & 0 & 0 \\ 0 & 0 & p_{max} & 0 & 0 & 0 \\ 0 & 0 & 0 & r_{max} & 0 & 0 \\ 0 & 0 & 0 & 0 & \phi_{max} & 0 \\ 0 & 0 & 0 & 0 & 0 & \psi_{max} \end{bmatrix} = \begin{bmatrix} 1 & 0 & 0 & 0 & 0 & 0 \\ 0 & \frac{\pi/180}{0.0059} & 0 & 0 & 0 & 0 \\ 0 & 0 & 1 & 0 & 0 & 0 \\ 0 & 0 & 0 & 1 & 0 & 0 \\ 0 & 0 & 0 & 0 & \pi/180 & 0 \\ 0 & 0 & 0 & 0 & 0 & \pi/180 \end{bmatrix}. \tag{7}$$

And the block $F_{ts} = F_t D_{dt}$, where D_{dt} is a diagonal matrix with each element corresponding to the span (the maximum value minus the minimum) of each disturbance input:

$$D_{dt} = \begin{bmatrix} v_{g_{max}} & 0 & 0 \\ 0 & p_{g_{max}} & 0 \\ 0 & 0 & r_{g_{max}} \end{bmatrix} = \begin{bmatrix} 7.65 & 0 & 0 \\ 0 & 0.42 & 0 \\ 0 & 0 & 0.36 \end{bmatrix}. \tag{8}$$

Let the scaled system model G_{ts} highlighted in Fig. 6:

$$\begin{aligned} \dot{x}_t(t) &= A_{ts} x_t(t) + B_{ts} u_t(t) \\ y_t(t) &= C_{ts} x_t(t). \end{aligned} \tag{9}$$

And let the scaled perturbation model G_{ds} also highlighted in Fig. 6:

$$\begin{aligned} \dot{x}_t(t) &= A_{ts} x_t(t) + F_{ts} d_t(t) \\ y_t(t) &= C_{ts} x_t(t). \end{aligned} \tag{10}$$

In that scaled system, the control objective regarding the disturbance rejection $|d(t)| \leq 1$ is to design u with $|u(t)| \leq 1$ such that $|e(t)| = |y(t) - r(t)| \leq 1$.
The disturbance rejection will not entail input saturation using acceptable control ($|e(t)| \leq 1$) if, for each disturbance input, each singular value of G_{ts} approximately satisfies [18]:

$$\sigma_i(G_{ts}) \geq |u_i^* g_{ds}| - 1, \text{ at frequencies where } |u_i^* g_{ds}| > 1 (0 \text{ dB}), \tag{11}$$

where u_i is the i-th output singular vector (column vector) of G_{ts} (from the singular value decomposition: $G_{ts} = U \Sigma V^*$), and g_{ds} is the vector of G_{ds} corresponding to the single disturbance input. The term $u_i^* g_{ds}$ may be interpreted as the projection of g_{ds} onto the i-th output singular value of the plant.
Figs. 7, 8 and 9 show that the lateral motion dynamics of the aircraft has controllability regarding the rejection of disturbances without saturating the inputs.

3.2 Disturbance rejection in the longitudinal motion

The same approach can be applied to the linearised state-state space model for the longitudinal model (Eq. 1).
Consider the diagram block shown in Fig. 6. However, for longitudinal motion, the scaled system model G_{ns} is given by:

$$\begin{aligned} \dot{x}_n(t) &= A_{ns} x_n(t) + B_{ns} u_n(t) \\ y_n(t) &= C_{ns} x_n(t), \end{aligned} \tag{12}$$

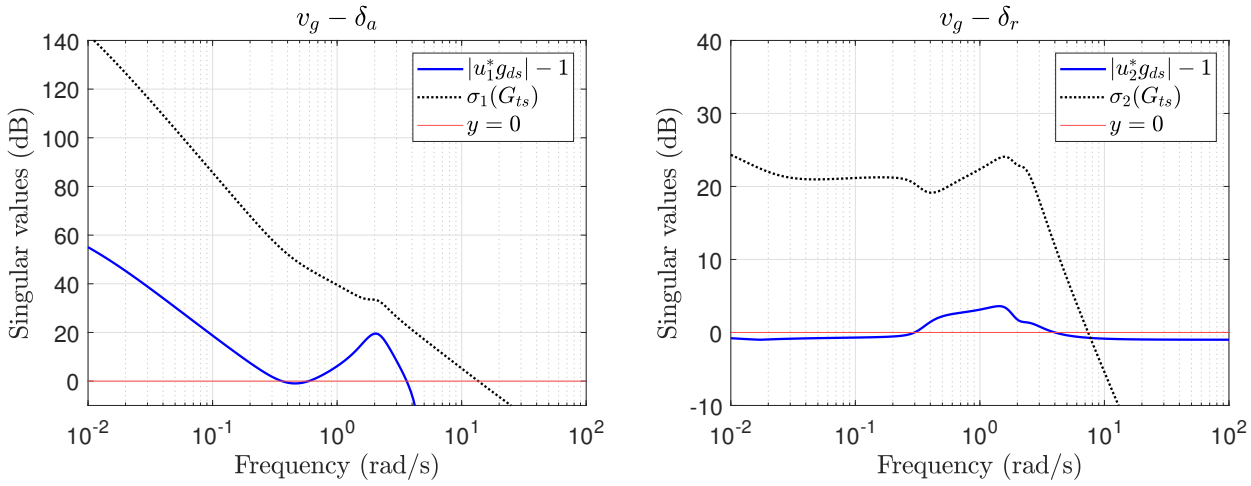

Figure 7 – v_g controllability

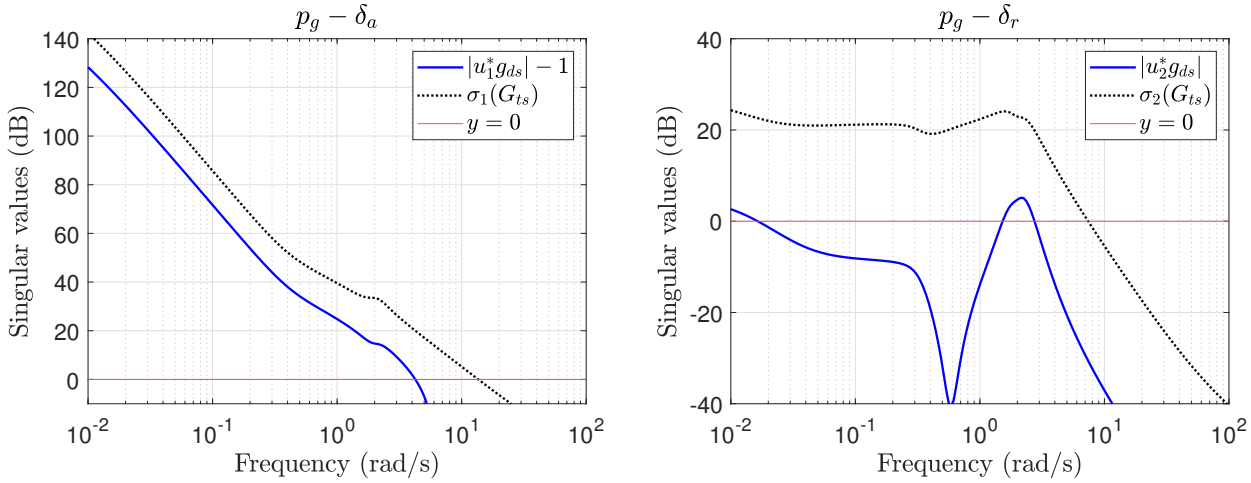

Figure 8 – p_g controllability

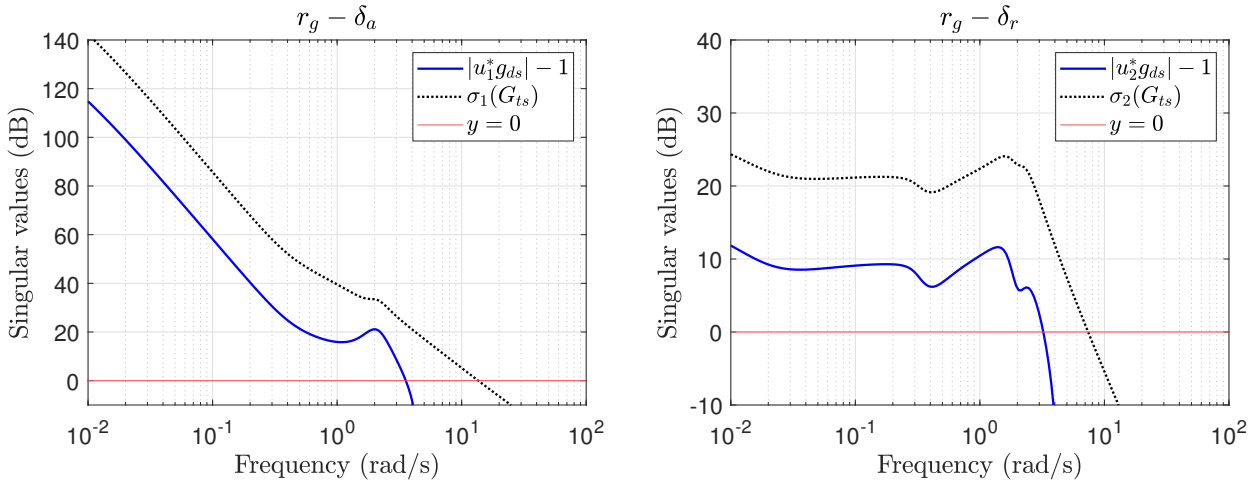

Figure 9 – r_g controllability

where, $B_{ns} = B_n D_{un}$, and D_{un} is a diagonal matrix with the maximum values of each input signal:

$$D_{un} = \begin{bmatrix} \delta_{e_{max}} & 0 \\ 0 & \delta_{t_{max}} \end{bmatrix} = \begin{bmatrix} 0.35 & 0 \\ 0 & 20 \end{bmatrix}. \tag{13}$$

The block $C_{ns} = D_{yn}^{-1} C_n$, where D_{yn} is a diagonal matrix with the maximum desired values of each

output signal: 1 degree (or $\pi/180$ rad) for the angle θ, 1 rad/s for angular velocity q, 1 m/s for linear velocities u and w, and 1 m for z_o and x_o. Thus,

$$D_{yt} = \begin{bmatrix} z_{o_{max}} & 0 & 0 & 0 & 0 & 0 \\ 0 & x_{o_{max}} & 0 & 0 & 0 & 0 \\ 0 & 0 & u_{max} & 0 & 0 & 0 \\ 0 & 0 & 0 & w_{max} & 0 & 0 \\ 0 & 0 & 0 & 0 & q_{max} & 0 \\ 0 & 0 & 0 & 0 & 0 & \theta_{max} \end{bmatrix} = \begin{bmatrix} 1 & 0 & 0 & 0 & 0 & 0 \\ 0 & 1 & 0 & 0 & 0 & 0 \\ 0 & 0 & 1 & 0 & 0 & 0 \\ 0 & 0 & 0 & 1 & 0 & 0 \\ 0 & 0 & 0 & 0 & 1 & 0 \\ 0 & 0 & 0 & 0 & 0 & \pi/180 \end{bmatrix}. \tag{14}$$

The scaled perturbation model G_{ds} is:

$$\begin{aligned} \dot{x}_n(t) =& A_{ns}x_n(t) + F_{ns}d_n(t) \\ y_n(t) =& C_{ns}x_n(t), \end{aligned} \tag{15}$$

where $F_{ns} = F_n D_{dn}$, and D_{dt} is a diagonal matrix with each element corresponding to the span (the maximum value minus the minimum) of each disturbance input:

$$D_{dt} = \begin{bmatrix} u_{g_{max}} & 0 & 0 \\ 0 & w_{g_{max}} & 0 \\ 0 & 0 & q_{g_{max}} \end{bmatrix} = \begin{bmatrix} 0.00 & 0 & 0 \\ 0 & 3.18 & 0 \\ 0 & 0 & 0.12 \end{bmatrix} \tag{16}$$

Then, the relation in Eq. 11 was applied to the scaled longitudinal model. It is worthy of note that u_g does not influence the aircraft dynamics.

Figs. 10 and 11 show that the longitudinal motion dynamics of the aircraft have controllability regarding the rejection of disturbances without saturating the inputs.

From the graph, it is possible to verify that there is a range where the δ_t is not able to deal with disturbance w_g. However, it probably will not cause an input saturation due to the low frequency and the narrow band. Even so, if we want to be conservative, the problem can be solved by modifying the engine to be more powerful or, as a workaround, to steer the aircraft to fly in tight formation avoiding the regions inside the vortex field where the values of w_g are high. From Fig.2, it is possible to infer that the region around the point $(y_o, z_o) = (0,0)$ should thus be avoided.

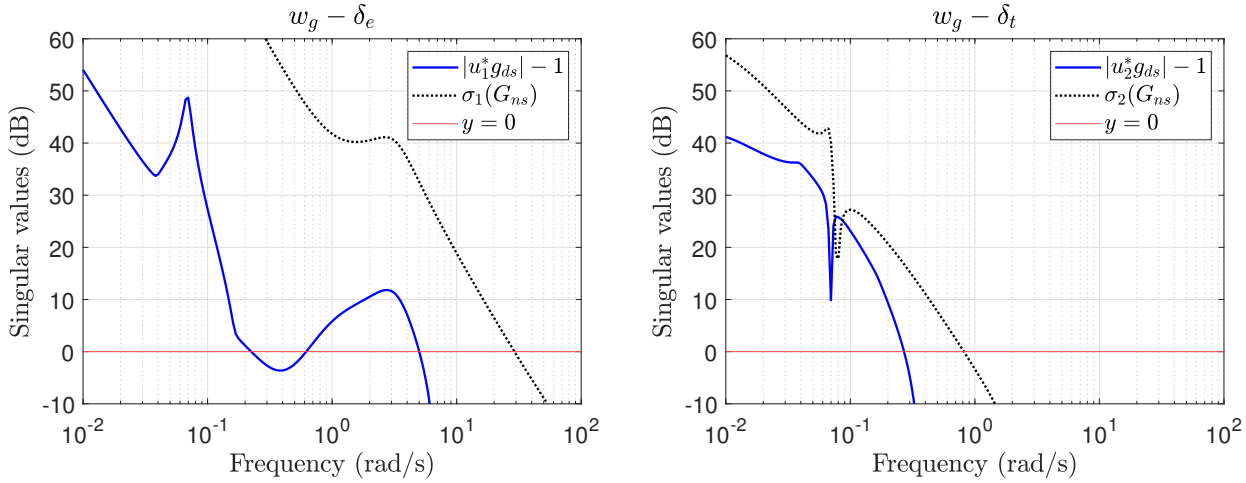

Figure 10 – w_g controllability

4. Trim Conditions

In order to analyse the fuel consumption of the wingman inside the vortex field as well as the behaviour of the variables of the aircraft, a trim algorithm was developed. Six conditions were considered as follows:

1. all the commands of the control surfaces are “free” as well the angles of the aircraft; the throttle is not locked to allow differential throttle.

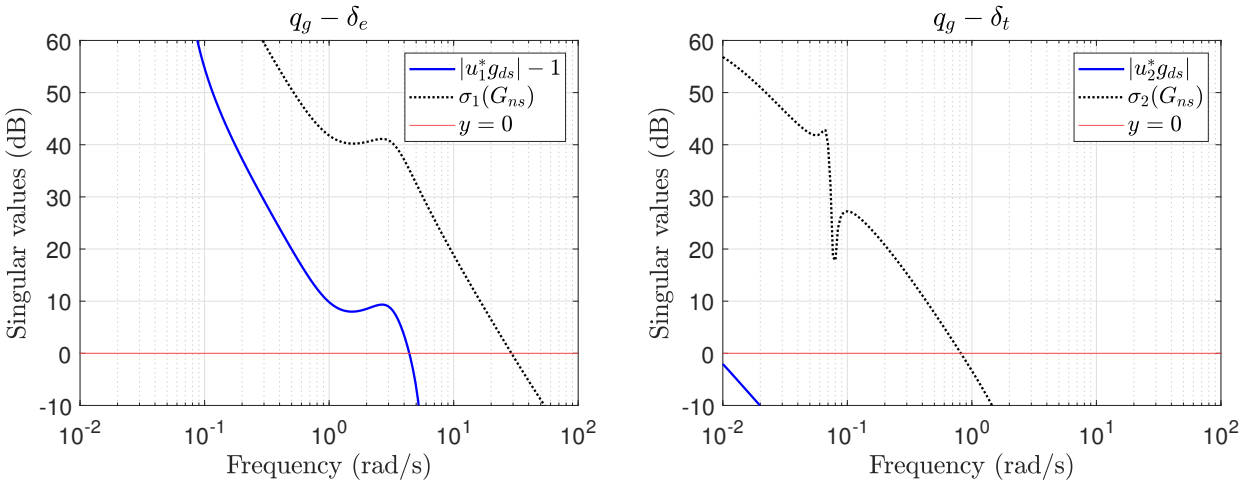

Figure 11 – q_g controllability

2. the same condition as the first one, but the throttle is locked to not allow differential throttle.
3. all the angles of the aircraft are locked at zero (yaw, roll, pitch, attack and sideslip); the throttle is not locked to allow differential throttle.
4. the same condition as the third one, but the throttle is locked to not allow differential throttle.
5. all the angles of the aircraft but pitch angle are locked at zero so to maintain level flight; the throttle is not locked to allow differential throttle.
6. the same condition as the fifth one, but the throttle is locked to not allow differential throttle.

The objective is to gain insight into a better approach to designing the controller of the aircraft inside the vortex and the setpoint controller to reach good results for fuel saving, safety, performance, and comfort.
The trim algorithm was formulated as a nonlinear optimization problem using the Eq. 1 as follows. That problem was solved numerically using an “interior-point” algorithm. To solve the trim algorithm, it was necessary to obtain a function using interpolation of the simulation data of the induced velocities due to the wake vortex. That function receives the y_o and z_o relative coordinates and provides the value of u_g, v_g, w_g, p_g, q_g and r_g.

$$
\begin{aligned}
\underset{x_p \in \mathbb{R}^{23}}{\text{minimize}} \quad & ff_{LH} + ff_{RH} \\
\text{subject to} \quad & [\, A_a \; B_a \,] x_p + F_a d_a(y_o, z_o) = 0; \\
& 0 \leq y_o \leq 30; \quad -15 \leq z_o \leq 15; \\
& -10 \leq v \leq 10; \\
& -10\pi/180 \leq \phi \leq 10\pi/180; \\
& -10\pi/180 \leq \psi \leq 10\pi/180; \\
& 10 \leq u \leq 10; \quad -10 \leq w \leq 10; \\
& -10\pi/180 \leq \theta \leq 10\pi/180; \\
& -40 \leq n_{1_{LH}} \leq 10; \quad -40 \leq n_{1_{RH}} \leq 10; \\
& -20\pi/180 \leq \delta_a \leq 20\pi/180; \\
& -15\pi/180 \leq \delta_r \leq 15\pi/180; \\
& -20\pi/180 \leq \delta_e \leq 20\pi/180; \\
& -50 \leq \delta_{t_{LH}} \leq 20; \quad -50 \leq \delta_{t_{RH}} \leq 20; \\
& p = 0; \; r = 0; \; q = 0; \; x = 0; \\
& \dot{n}_{1_{LH}} = 0; \; \dot{n}_{1_{RH}} = 0;
\end{aligned}
\tag{17}
$$

where $x_p = [x_a \; u_a]^T$ is a vector comprising the state and input variables (incremental values).
For cases 1 and 2, the restrictions were used as specified above. For the cases 3 and 4, the angles β (through v), ϕ, θ and ψ were set to zero. For cases 5 and 6, only the pitch angle was not set to zero. Cases 1, 3 and 5 use the model of the aircraft with the differential throttle. Cases 2, 4 and 6 have the matrices A_a, B_a and F_a modified so that only one throttle command is necessary to act at both sides of the aircraft engines.

4.1 Results and analysis based on graphs

This section presents the results by means of graphs of the variable in relation to the relative positions y_o and z_o for all the aforementioned cases.
First, the fuel consumption inside the vortex field is shown in Figs. 12 and 13. The shapes are very similar, however in cases 3 and 4 the fuel savings are a bit lower. The graphs in cases 4 and 6 present several local minima around the level curve where the fuel flow increment is zero, whereas in the other cases there is only one local minimum which is the global minimum. Therefore, the use of an extremum-seeking algorithm will not be effective in cases 4 and 6.
The increase in the pitch angle has an interesting profile, as its minimum value is almost at the "sweet spot" and the format resembles the previous graphs but with the axes exchanged (see Fig. 14 and 15). The profiles of each case are quite similar; however, as in the fuel savings graph, case 6 has several minima points around the level curve of zero increments.
The increase in the roll angle has similar shapes in cases 1 and 2 in Figs. 16 and 17, with some negative and positive peaks which should be avoided while manoeuvring inside the vortex field.
The increase in the yaw angle has low values in almost all the vortex fields, as can be seen in Figs. 18 and 19. It would be important to avoid the regions where abrupt variations could appear at the yaw angle (see the peaks in the graph). However, the peak values are very low in cases 1 and 2.
In Figs. 20 and 21, all cases present a very similar shape and low values. It is noteworthy the great variation between the maximum and minimum peak near the "sweet spot" at $z_o = 0$.
The increase in rudder angle is shown in Figs. 22 and 23. The most well-behaved shapes are found in cases 1 and 2. However, in all cases, inside all the vortex fields, the values are not high.
The increase in elevator angle has low values inside the vortex field, as can be seen in Figs. 24 and 25. However, cases 3, 4 and 6 show a not well-behaved shape.
The graphs for an increase in throttles of left and right-hand sides when using differential throttle are shown in Figs. 26 and 27. Cases 3 and 5 show a not well-behaved shape.
The throttle with left-hand and right-hand commands locked to obtain a unique signal for the engines is shown in Fig. 28. Cases 4 and 6 have a not well-behaved shape.

4.2 Results and analysis based on consolidated table

For each case, the coordinates of the "sweet spot" were computed using the optimization algorithm and the values of the variables at that point. Table 1 shows the results. N/A stands for not applied for that case, and b is the aircraft wingspan of 21.5 m. The algorithm presented difficulties to find the "sweet spot" in cases 4 and 6 due to the presence of several minima in the function.
One can observe that the location of the "sweet spot" is not so different for each case. Fuel savings are a little lower in cases 3 and 4. The roll, pitch and yaw angles have low values even when they are not locked to zero. And, in all cases, the control surfaces have low values as well.
It is noteworthy that the results achieved here are not unique. It means that other values for the angles can be reached in the "sweet spot" and inside the vortex field. It is explained by the fact that the aircraft is underactuated, i.e., there are only four inputs to control, and at least, twelve outputs. However, the results shown are true if a setpoint control is used as an extremum-seeking controller enabling the wingman in tight formation flight to save maximum fuel while moving inside the vortex field.
Therefore, taking into account the analyses carried out with the aim of the trim algorithm, the recommended choice is Case 2: all the angles and control surfaces "free" and one throttle signal to command both the engines on the right-hand and left-hand sides.
Cases 1, 3 and 5 use a differential throttle which brings additional hurdles: the response of the aircraft to a differential throttle is very slow which is not suitable for flying inside the vortex. Even so,

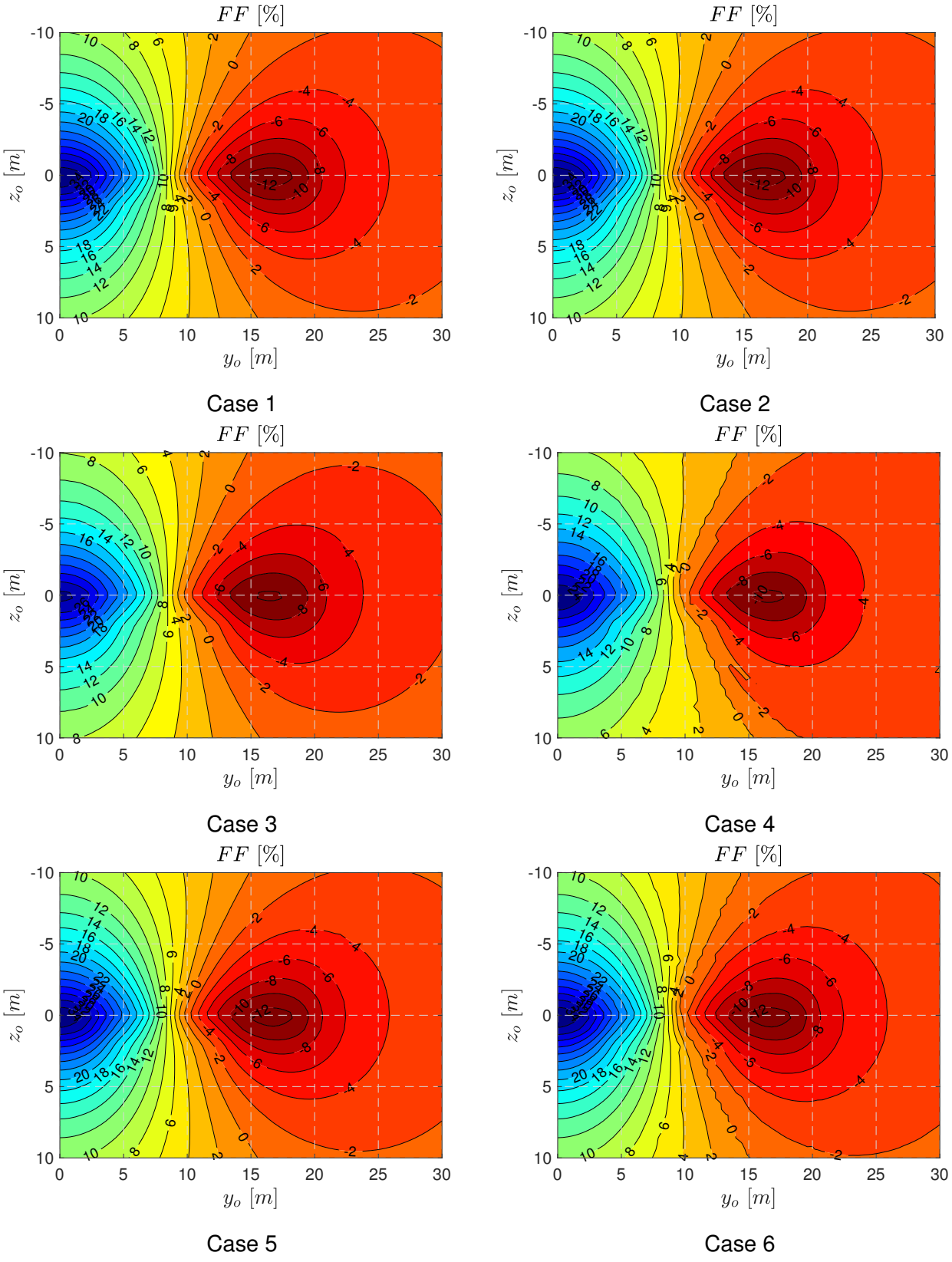

Figure 12 – Increase in fuel consumption

according to [19] and [20] the differential throttle can be used as a fail-safe mechanism for the vertical stabilizer in flights that are not in tight formation. Also, the fuel consumption inside the vortex field would be different on both sides of the aircraft so the fuel had to be shifted from one tank to the other. And high values of throttle found in Fig. 26 show saturation of the input signals.
Cases 4 and 6 present several local minima and would be a problem when using an extremum-

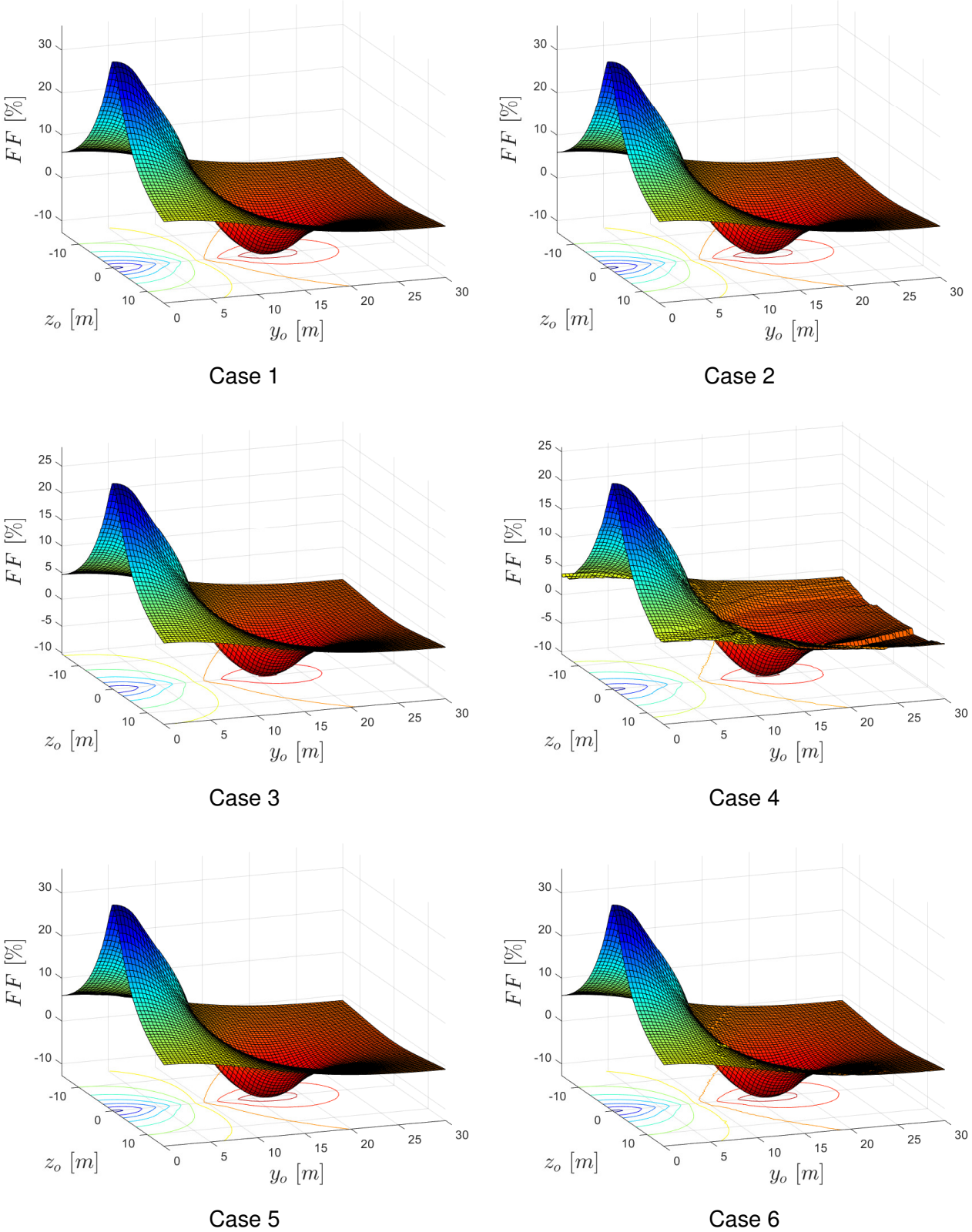

Figure 13 – Increase in fuel consumption

seeking controller which could be stuck at one of these points.
Furthermore, it is necessary to set a path to manoeuvre the wingman inside the vortex field to avoid some regions that could lead to an abrupt variation of the aircraft angles. As seen in Section 3.2, flying in some regions lead to the saturation of a control surface (the elevator) which could lead to aircraft instability.

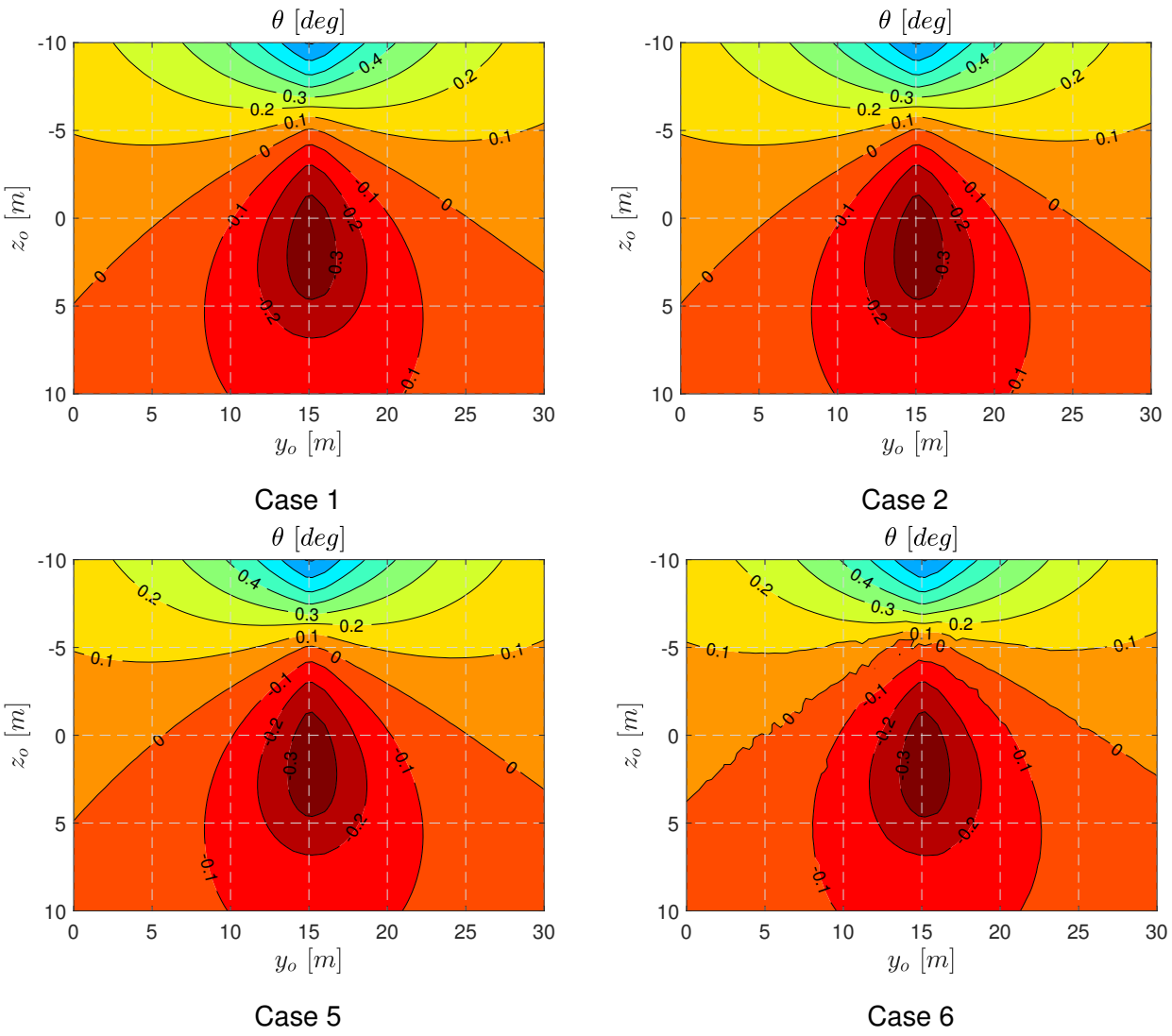

Figure 14 – Increase in pitch angle

Table 1 – Variables at the “sweet spot”

Variable	Unit	Case 1	Case 2	Case 3	Case 4	Case 5	Case 6
y_o	[m]	16.000	16.403	16.300	16.301	16.401	15.000
y_o/b	—	0.744	0.763	0.758	0.758	0.763	0.698
z_o	[m]	0.000	0.000	0.000	0.000	0.000	0.000
z_o/b	—	0.000	0.000	0.000	0.000	0.000	0.000
$ff_{LH} + ff_{RH}$	[%]	-12.92	-12.98	-10.43	-10.56	-12.98	-12.43
ϕ	[deg]	0.000	0.000	0.000	0.000	0.000	0.000
ψ	[deg]	-0.003	0.007	0.000	0.000	0.000	0.000
θ	[deg]	-0.374	-0.378	0.000	0.000	-0.378	-0.356
δ_a	[deg]	-0.257	-0.529	-0.460	-0.461	-0.525	0.453
δ_r	[deg]	-0.214	-0.211	-0.211	-0.211	-0.200	-0.239
δ_e	[deg]	0.080	0.054	-0.516	-0.501	0.067	0.128
$\delta_{t_{LH}}$	[deg]	-1.588	N/A	-1.278	N/A	-1.509	N/A
$\delta_{t_{RH}}$	[deg]	-1.588	N/A	-1.284	N/A	-1.681	N/A
δ_t	[deg]	N/A	-1.595	N/A	-1.297	N/A	-1.527
α	[deg]	-0.374	-0.378	-0.256	-0.262	-0.378	-0.356
β	[deg]	0.000	0.000	0.000	0.000	0.000	0.000
n_z	—	-0.120	-0.122	-0.100	-0.101	-0.122	-0.113

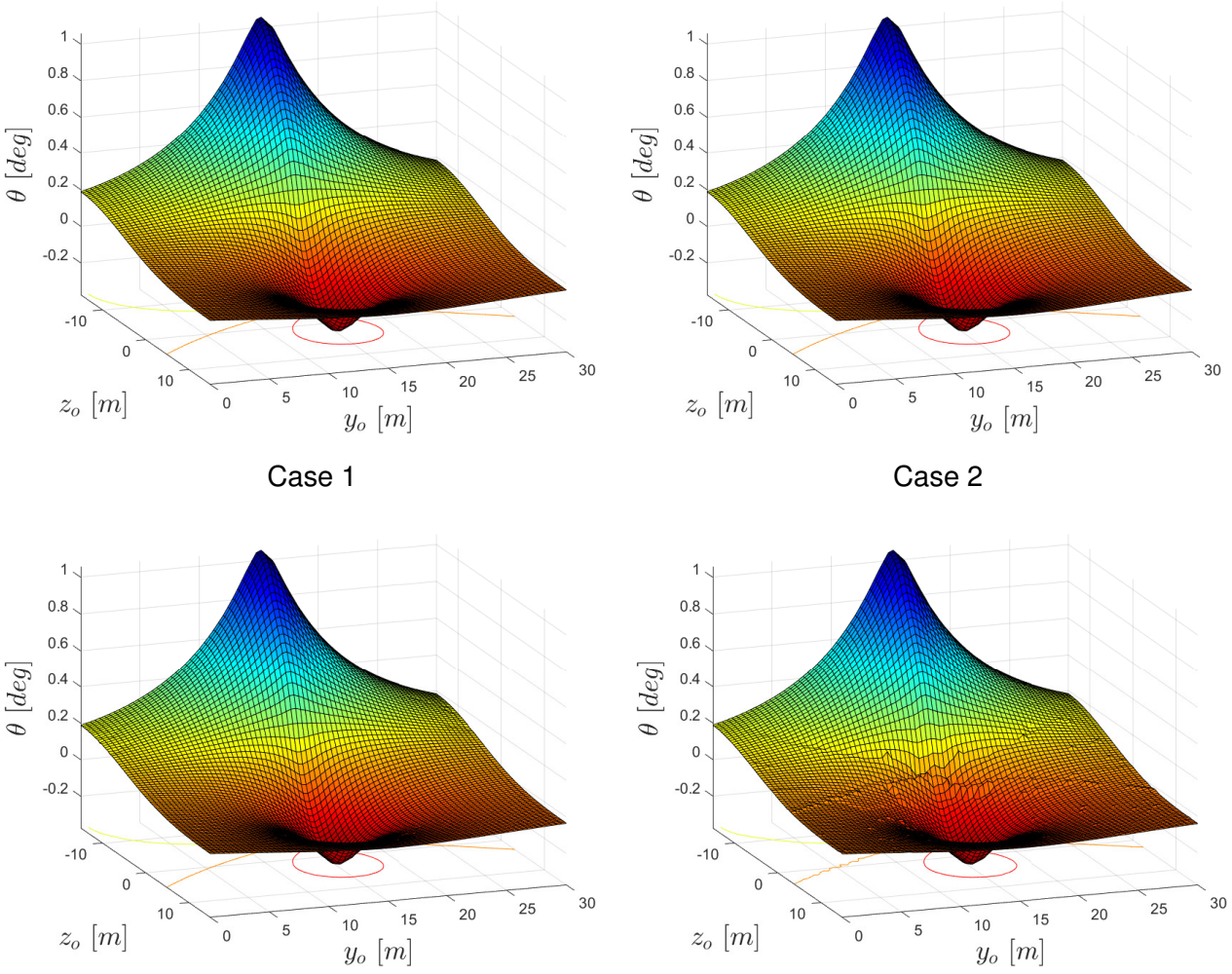

Case 1 Case 2

Case 5 Case 6

Figure 15 – Increase in pitch angle

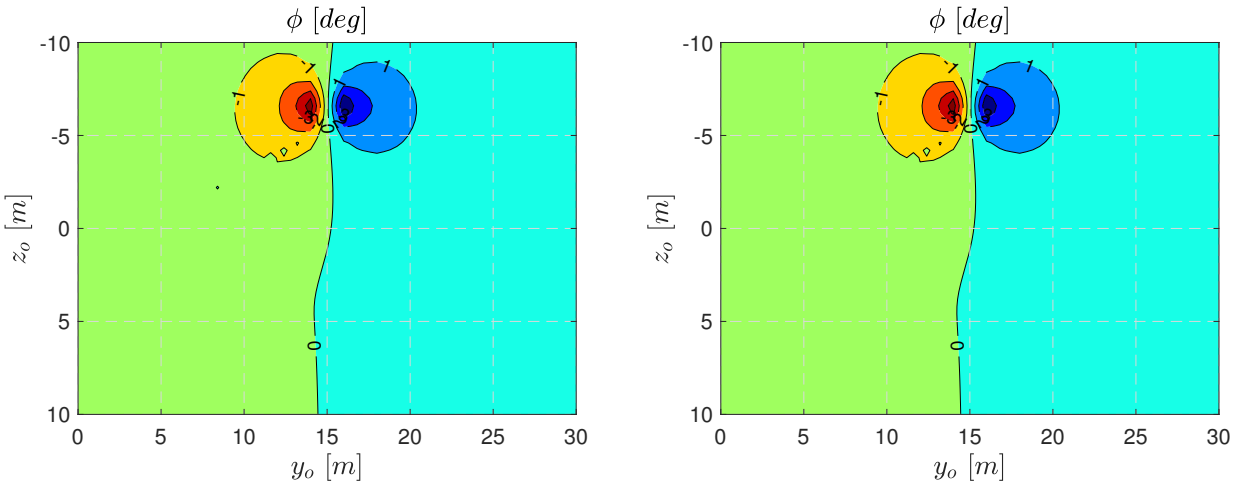

Case 1 Case 2

Figure 16 – Increase in roll angle

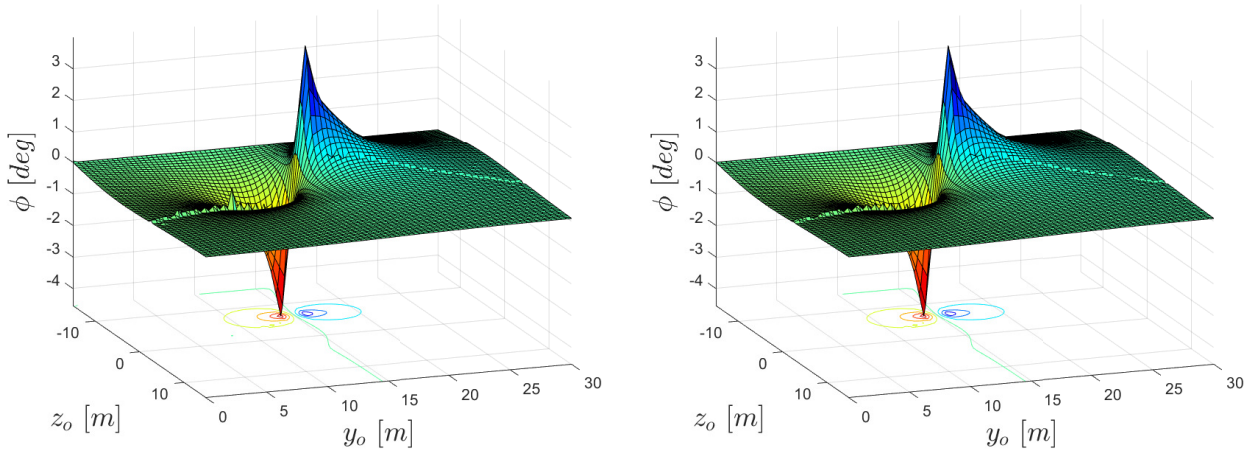

Case 1 Case 2

Figure 17 – Increase in roll angle

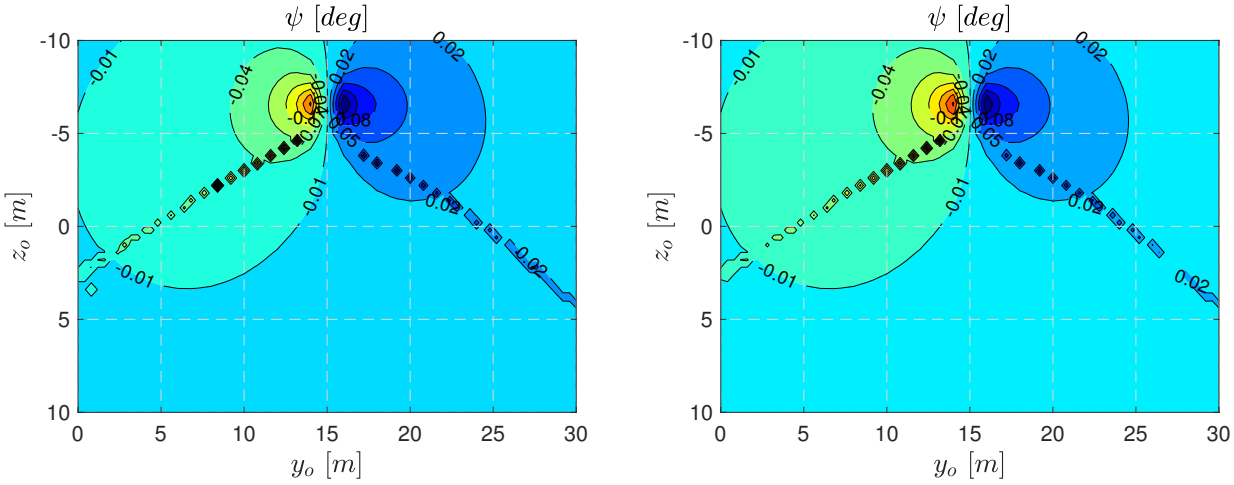

Case 1 Case 2

Figure 18 – Increase in yaw angle

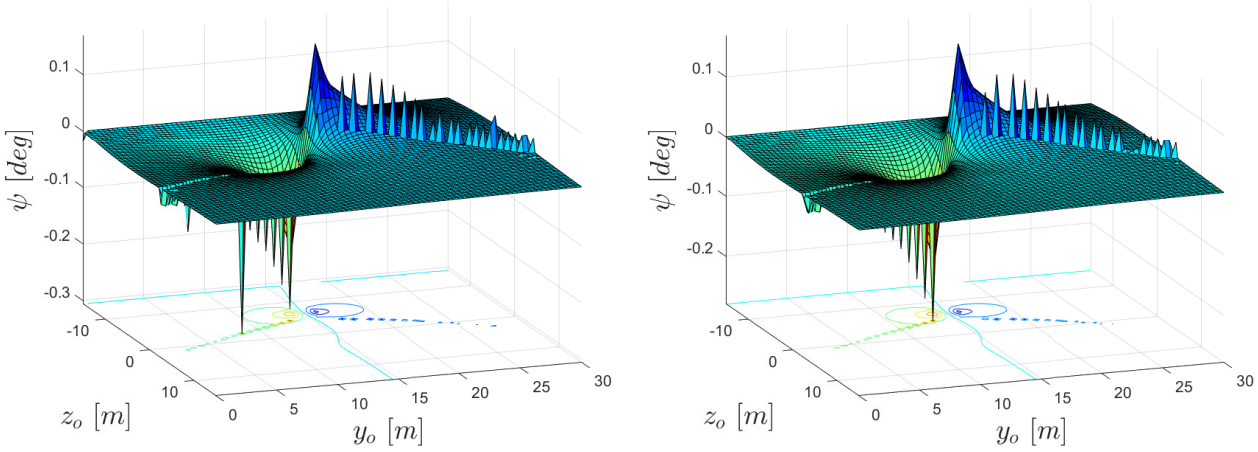

Case 1 Case 2

Figure 19 – Increase in yaw angle

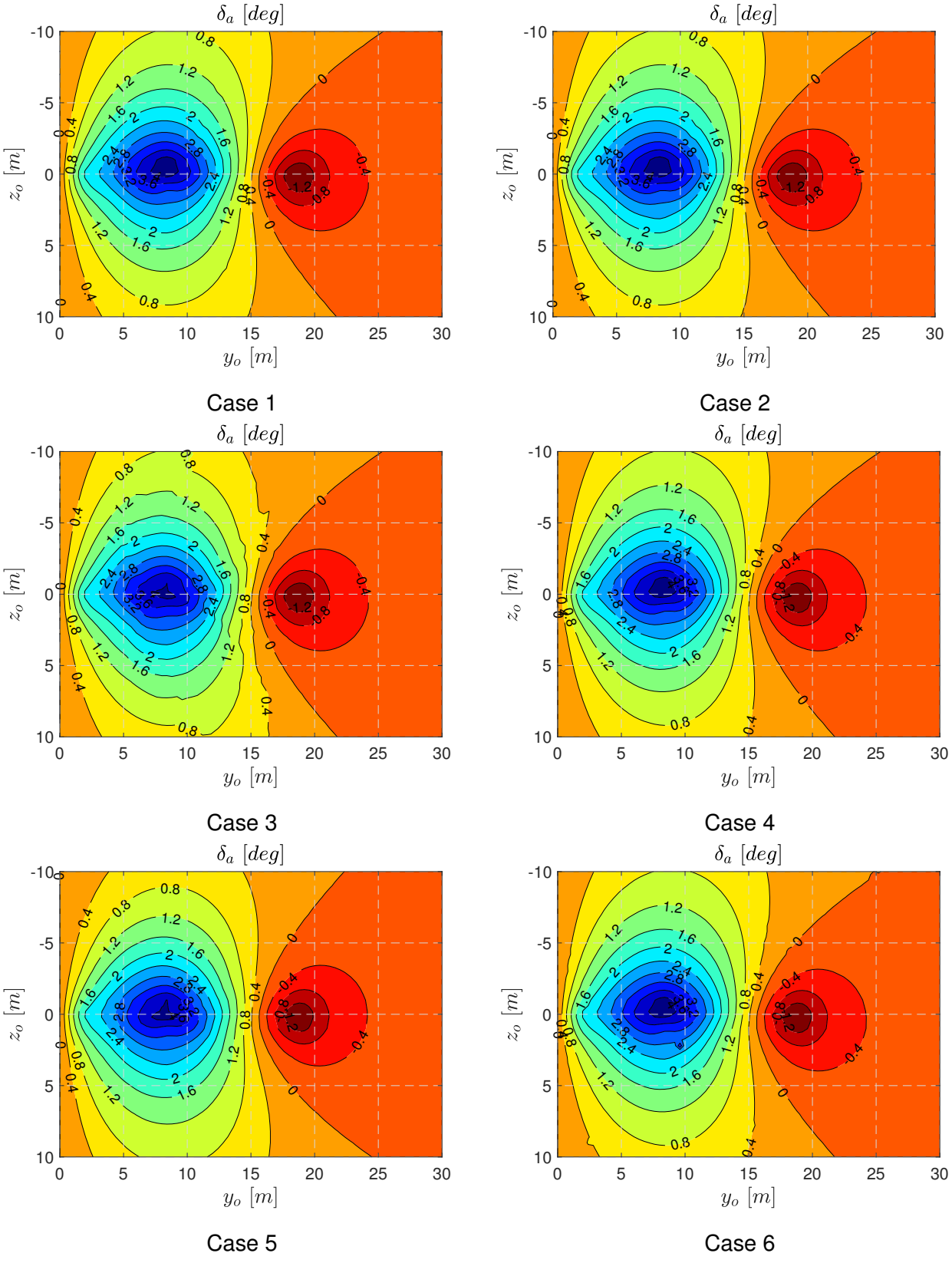

Figure 20 – Increase in aileron angle

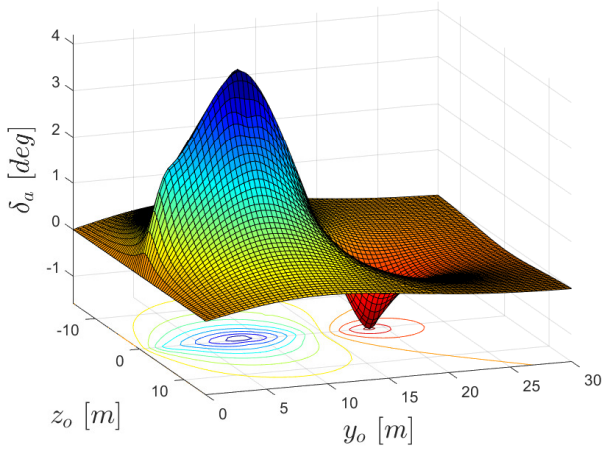

Case 1

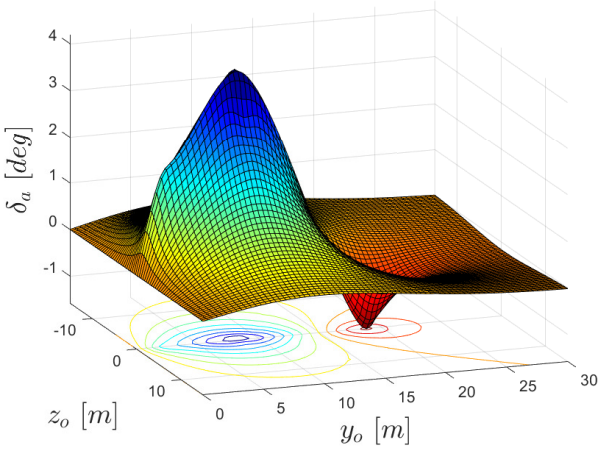

Case 2

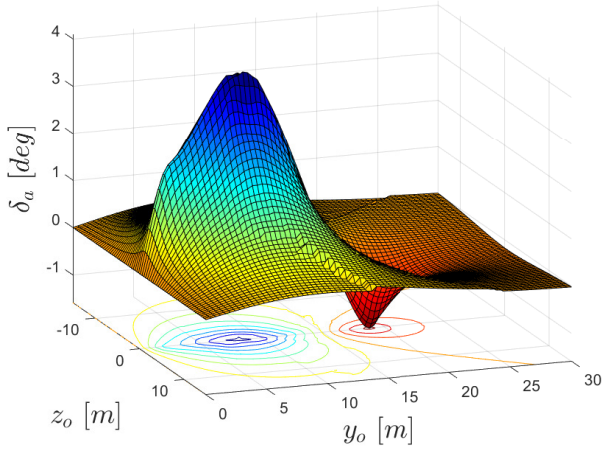

Case 3

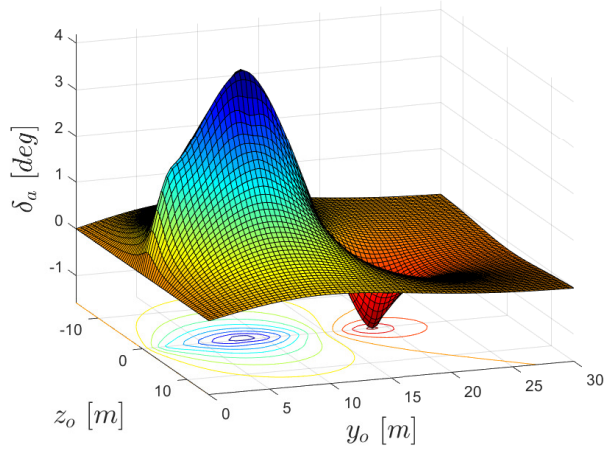

Case 4

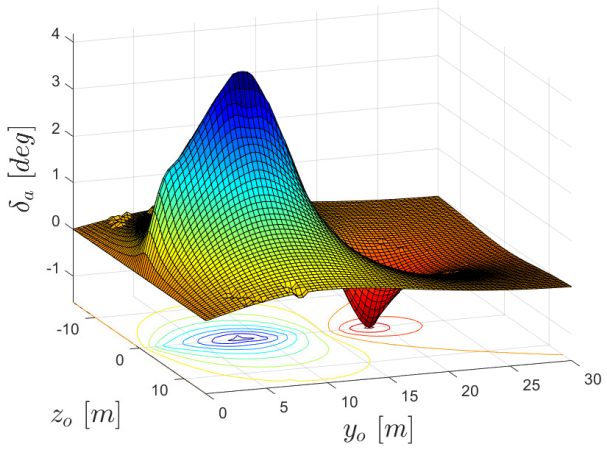

Case 5

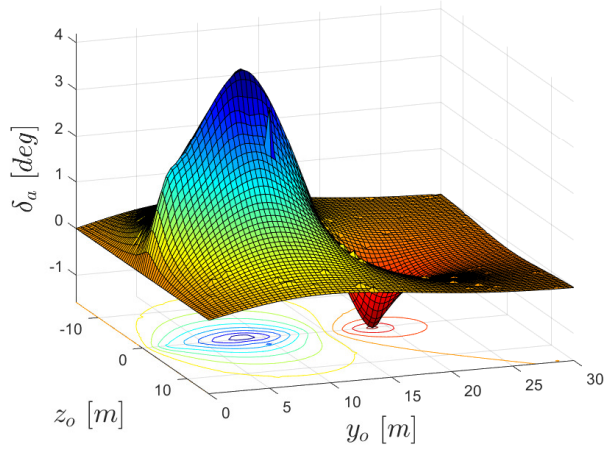

Case 6

Figure 21 – Increase in aileron angle

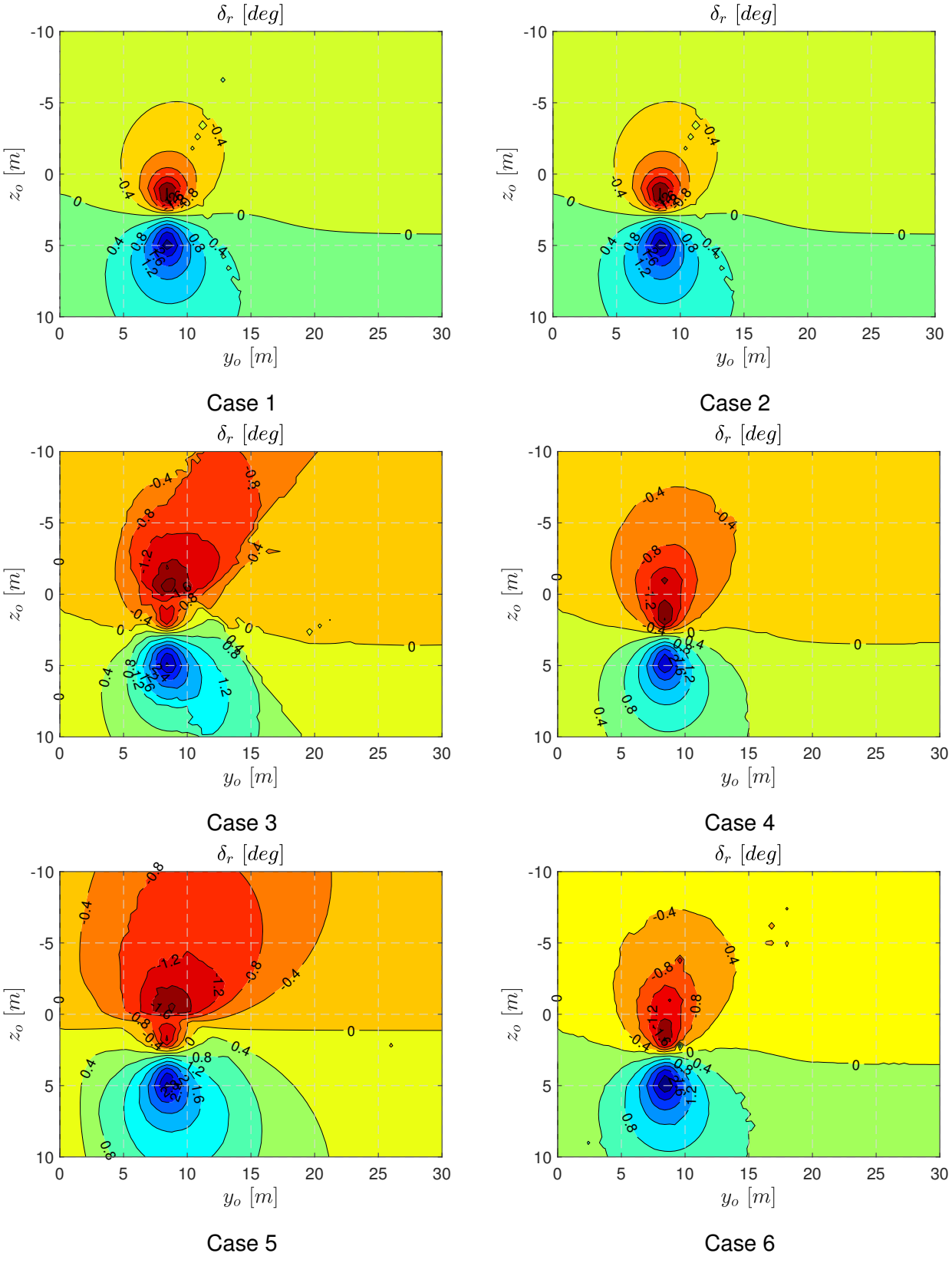

Figure 22 – Increase in rudder angle

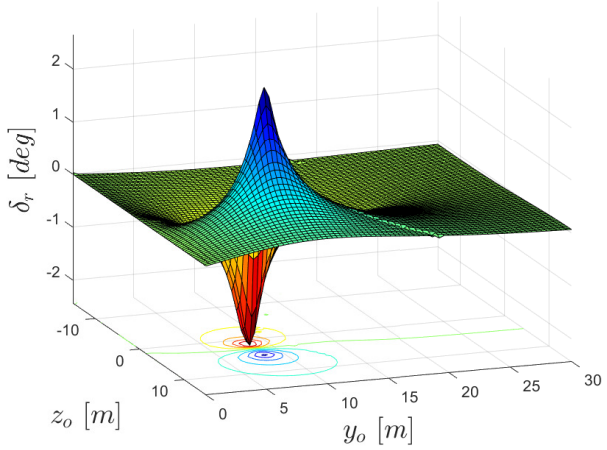

Case 1

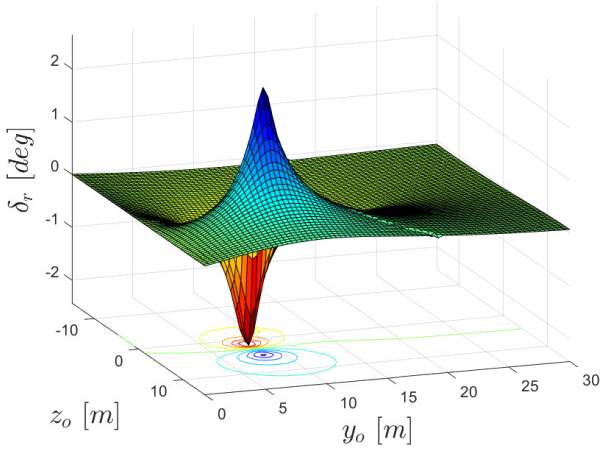

Case 2

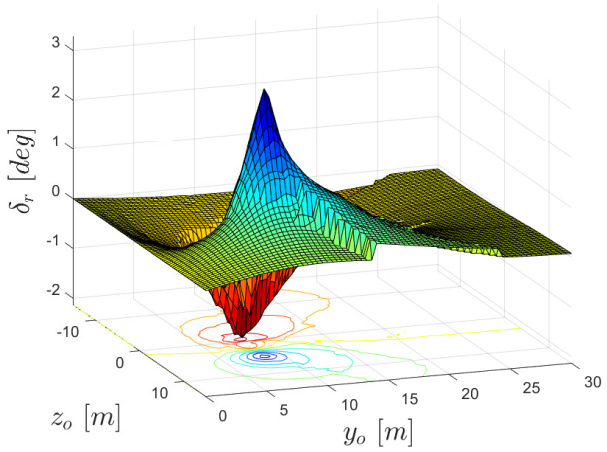

Case 3

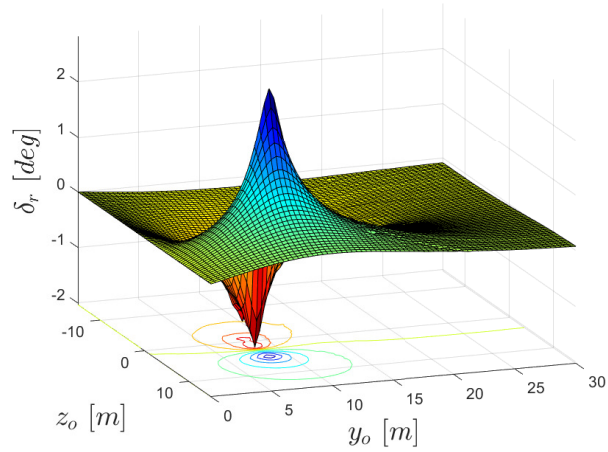

Case 4

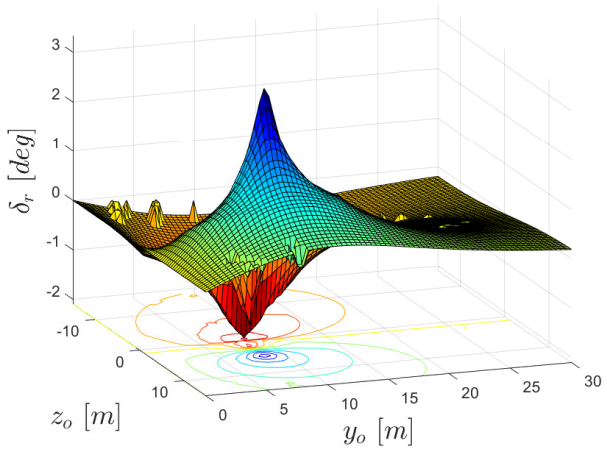

Case 5

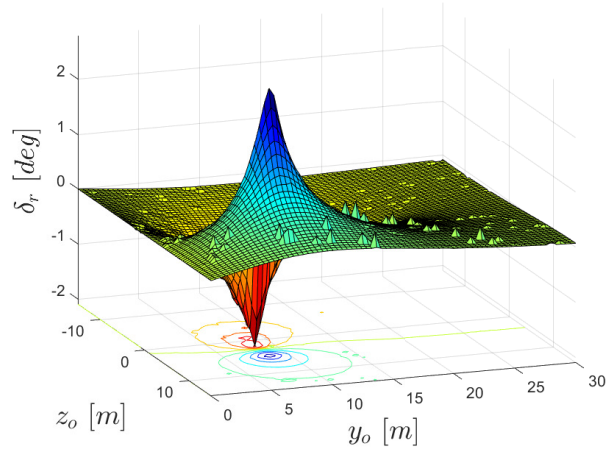

Case 6

Figure 23 – Increase in rudder angle

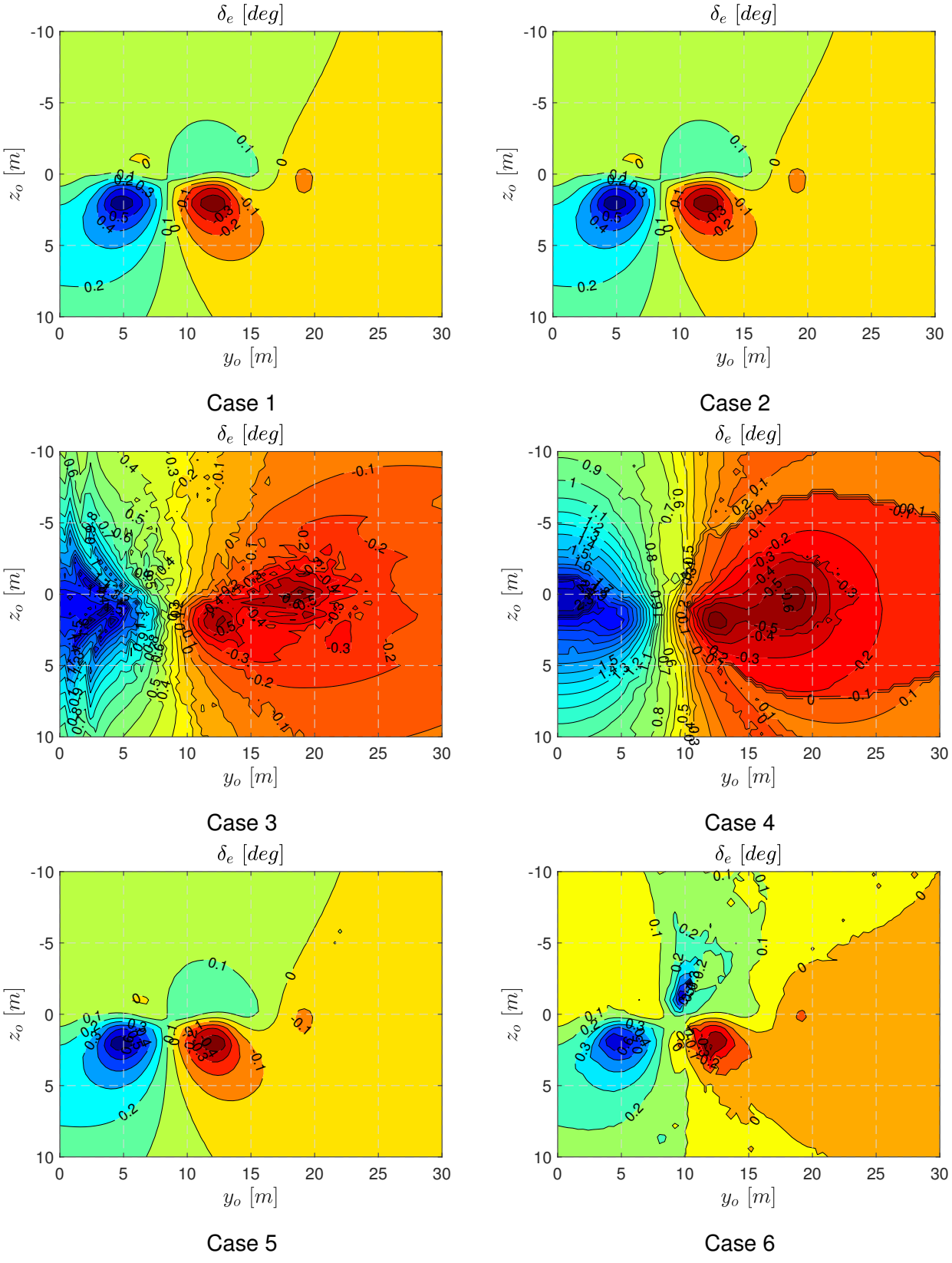

Figure 24 – Increase in elevator angle

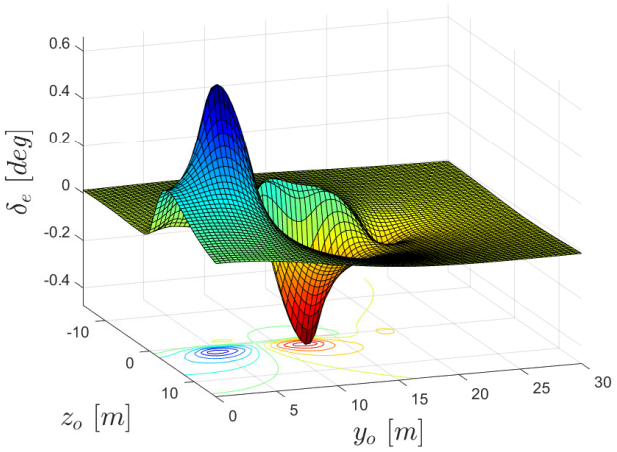

Case 1

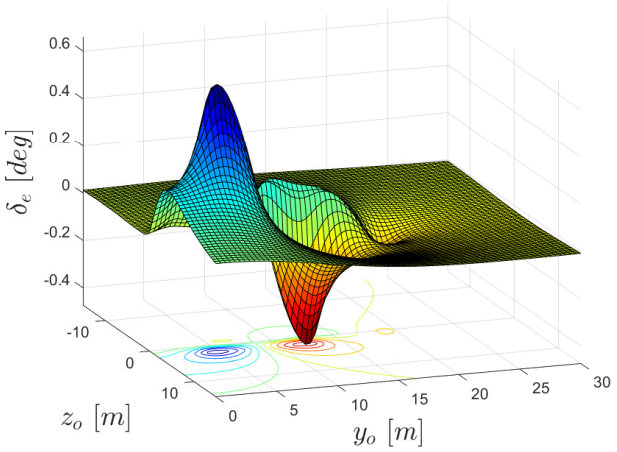

Case 2

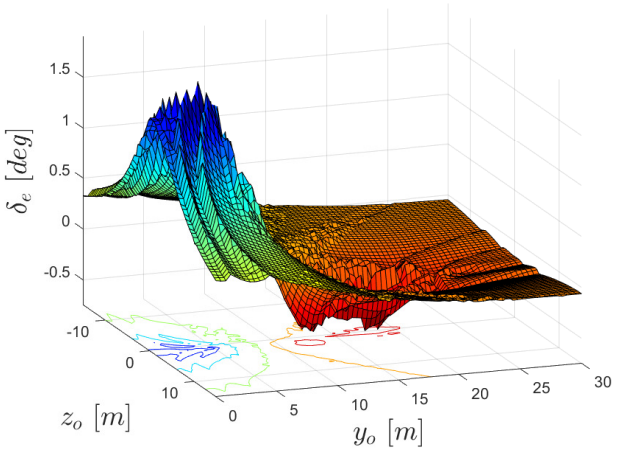

Case 3

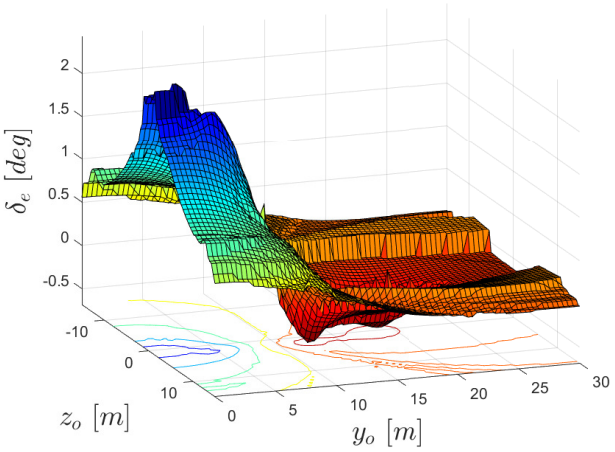

Case 4

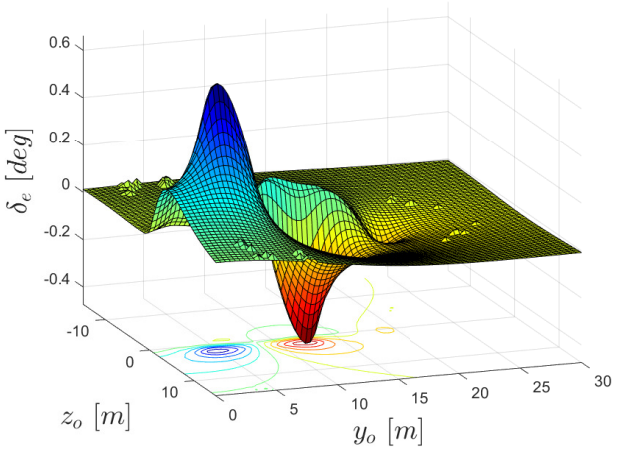

Case 5

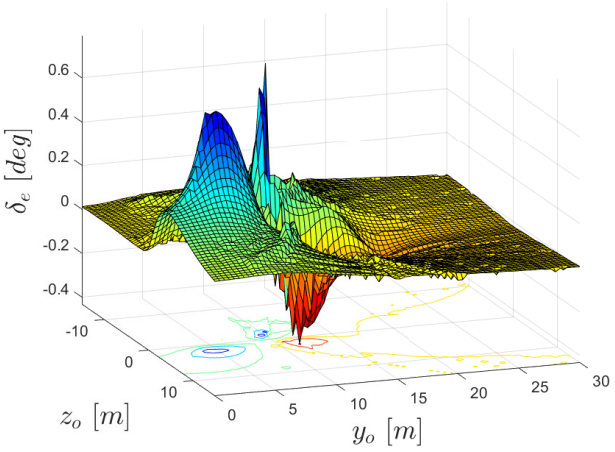

Case 6

Figure 25 – Increase in elevator angle

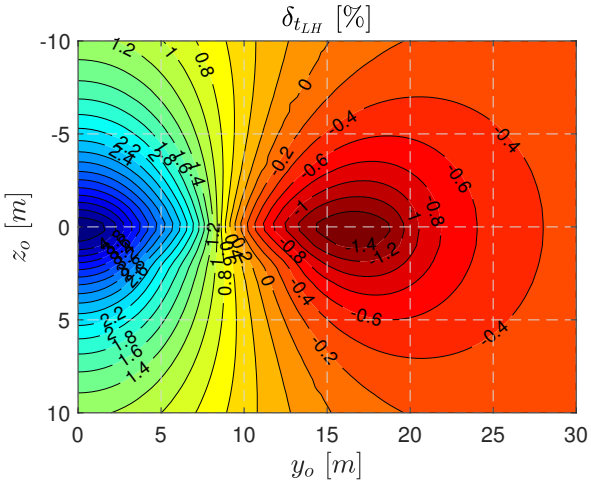

Case 1 - left-hand side

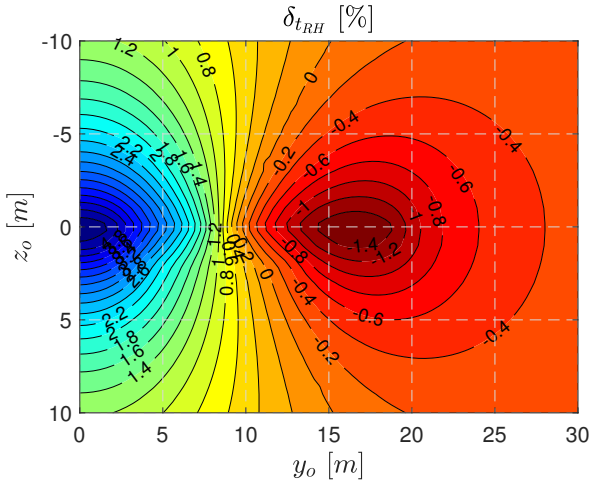

Case 1 - right-hand side

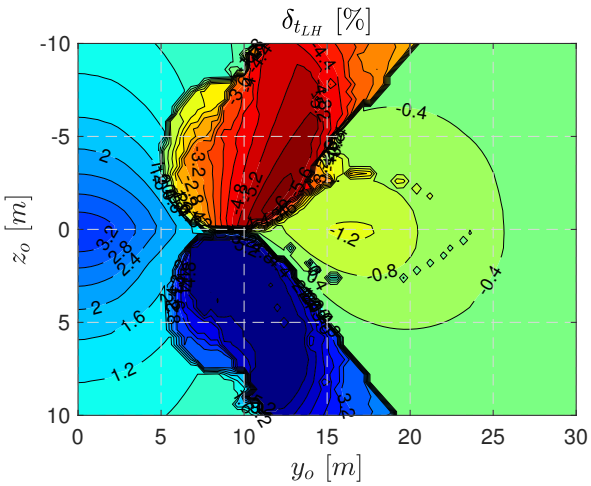

Case 3 - left-hand side

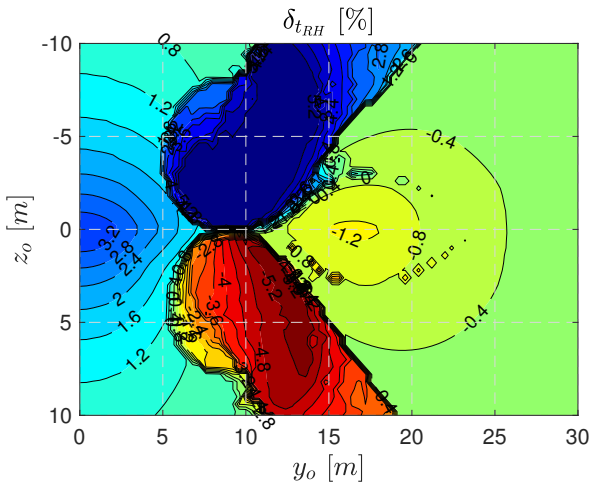

Case 3 - right-hand side

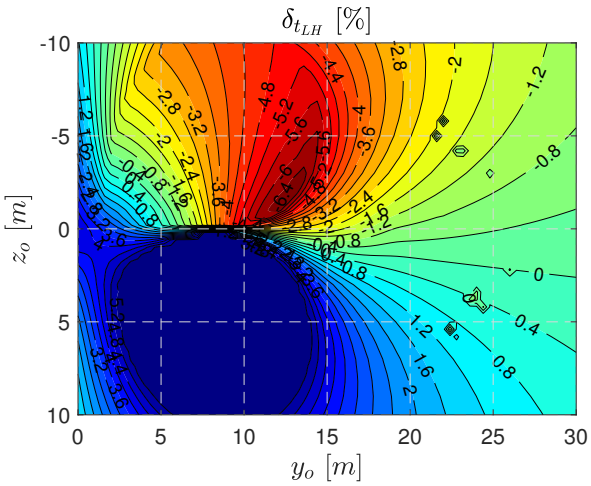

Case 5 - left-hand side

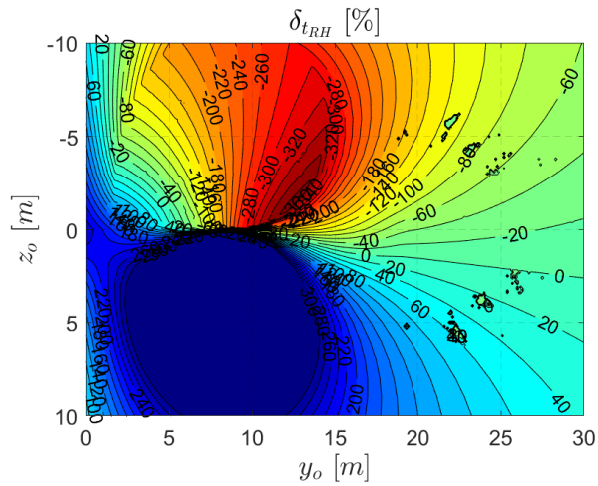

Case 5 - right-hand side

Figure 26 – Increase in throttle - left-hand and right-hand sides

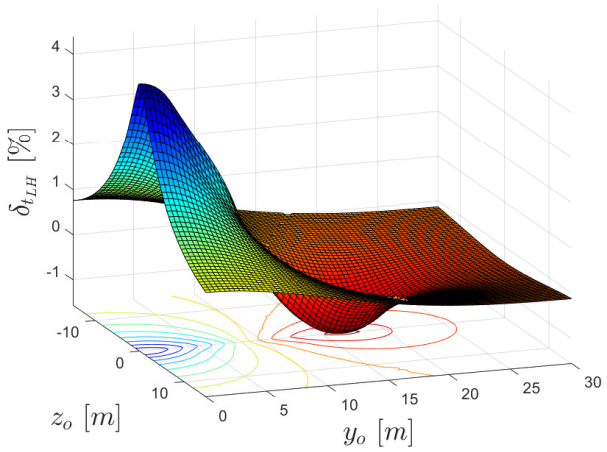

Case 1 - left-hand side

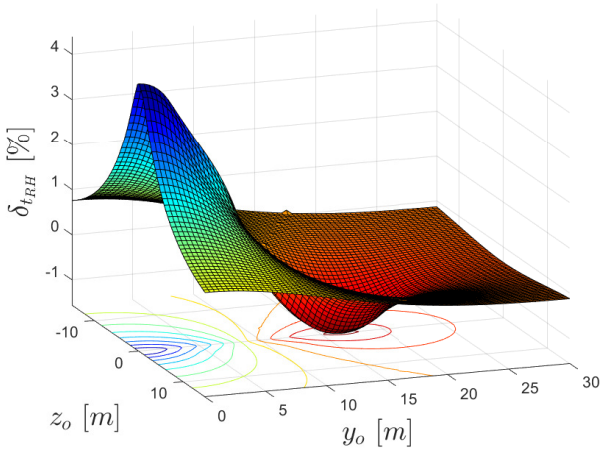

Case 1 - right-hand side

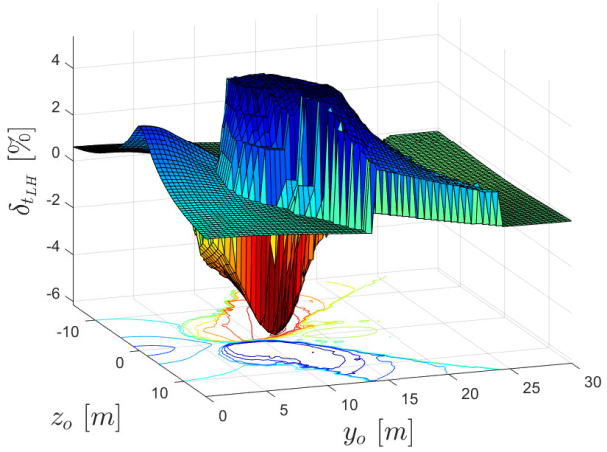

Case 3 - left-hand side

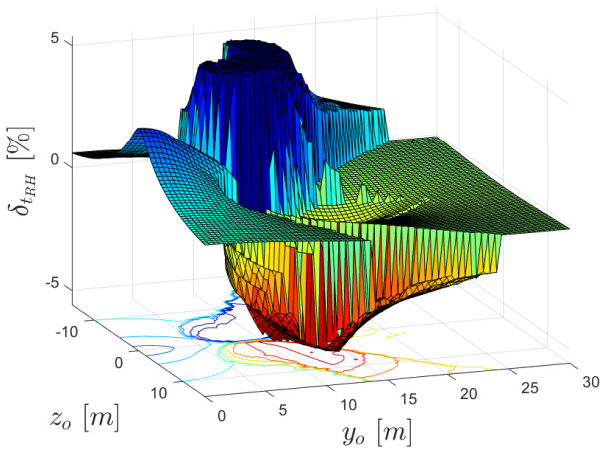

Case 3 - right-hand side

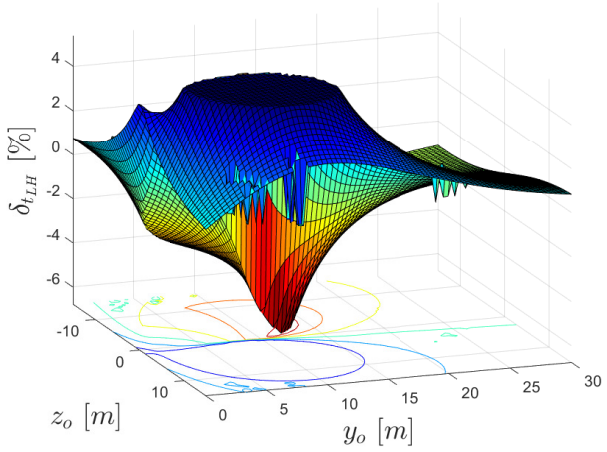

Case 5 - left-hand side

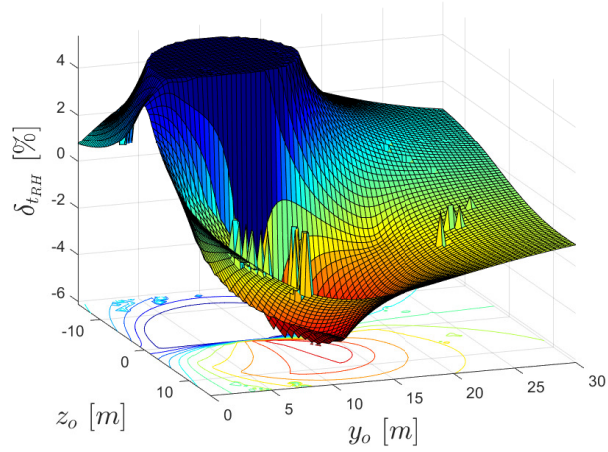

Case 5 - right-hand side

Figure 27 – Increase in throttle - left-hand and right-hand sides

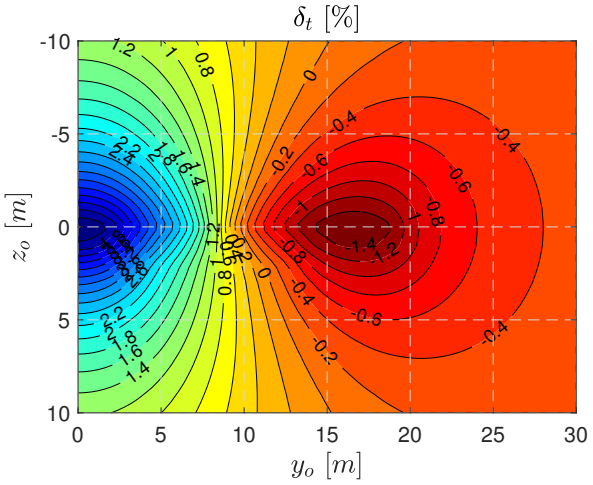

Case 2

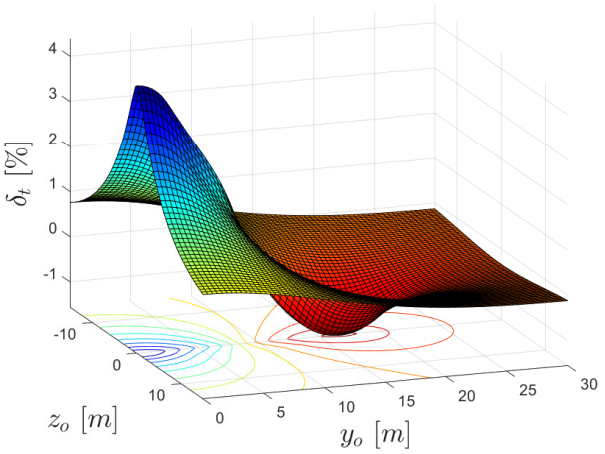

Case 2

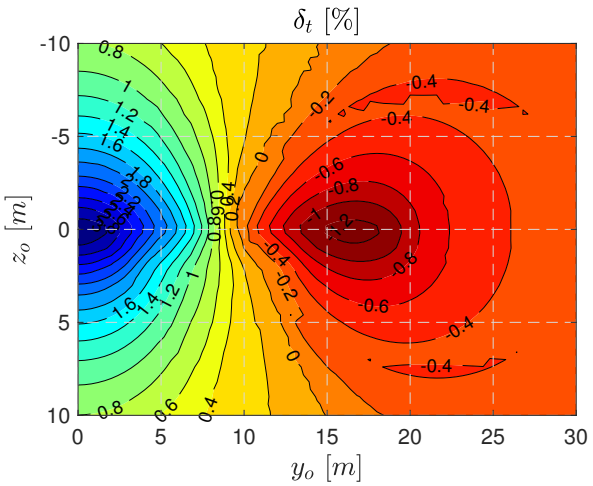

Case 6

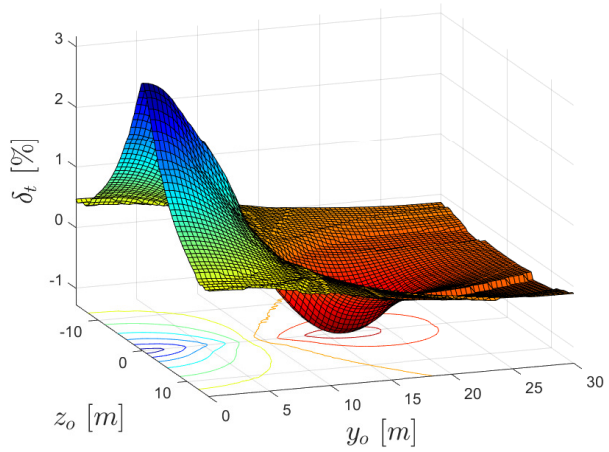

Case 6

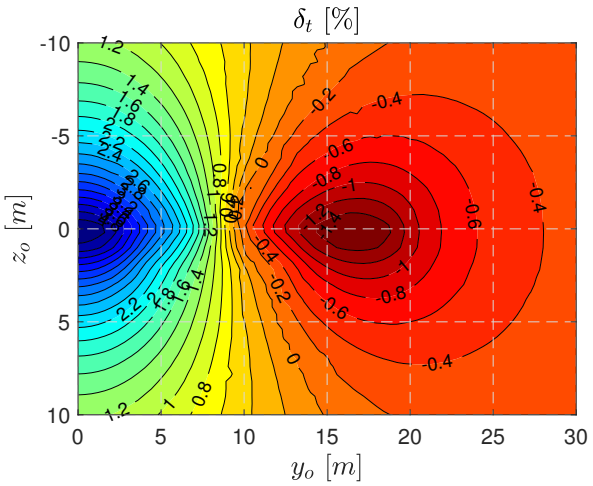

Case 6

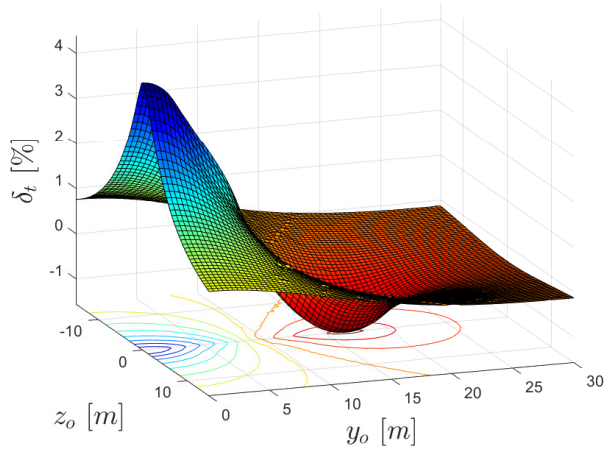

Case 6

Figure 28 – Increase in throttle - locked

5. Final Considerations

Considering the scenario of two medium-size cargo aircraft, the disturbances from the vortex encounter were incorporated into the model and analyses were carried out showing that these disturbances could be rejected without causing input saturation i.e., it is possible to control the aircraft inside the vortex using the control surfaces - aileron, rudder, elevator - and the thrust system of the aircraft. A trim algorithm was applied to different conditions. Findings showed that the use of the differential throttle is not suitable and the angles of the aircraft cannot be forced to zero inside the vortex by the control system (e.g. levelled flight). In some of these cases, there are regions where inputs can saturate, also there are some discontinuities in angles which can be viewed in the graphs. In all cases, it is necessary to avoid certain regions inside the vortex field. For the best case (angles free and the differential throttle locked), the region with maximum fuel saving is pointed out in the graph ($y_o = 16.4; z_o = 0$) with a fuel flow of -12.98% in this flight condition (aircraft dynamics, airspeed, altitude, cruise flight). The values of the variables at the "sweet spot" were founded for each case.
Some issues can be pursued in future works regarding the analysis of flight inside the vortex field: what are the conditions of flight for other scenarios (e.g. different models of leader and wingman aircraft) and what change of aircraft parameter influences the most (e.g. flight altitude, airspeed, aircraft size, propulsion system, aircraft shape); analysis of the flight in the vortex field when the leader is not at cruise flight was not addressed here. Regulatory and standardization issues can be addressed with a discussion about which parameters from the vortex influence analysis and the control system can be used to assure a safe flight inside the vortex with robust stability and performance.

6. Contact Author Email Address

For more information, please mail to: daniel.rossato@sp.senai.br or kienitz@ieee.org.

7. Copyright Statement

8. Acknowlegment

The second author acknowledges partial support through grant CNPq # 304557/2021-8.

References

[1] C. Wieselsberger. Beitrag zur erklärung des winkelfluges einiger zugvögel. *Zeitschrift fäur Flugtechnik und Motorluftschiffahrt*, 5:225–229, 1914.

[2] D. Hummel. The use of aircraft wakes to achieve power reduction in formation flight. In *Proceedings of the Fluid Dynamics Panel Symposium*, pages 1777–1794, Trondheim, May 1996. AGARD.

[3] M.Jake Vachon, Ronald J. Ray, Kevin R. Walsh, and Kimberly Ennix. F/a-18 aircraft performance benefits measured during the autonomous formation flight project. In *AIAA Atmospheric Flight Mechanics Conference and Exhibit*, Monterey, CA, August 2002. AIAA.

[4] E. Wagner, D. Jacque, W. Blake, and M. Pachter. Flight test results of close formation flight for fuel savings. *AIAA Atmospheric Flight Mechanics Conference and Exhibit*, 2002.

[5] Joe Pahle, Dave Berger, Mike Venti, Chris Duggan, Jim Faber, and Kyle Cardinal. An initial flight investigation of formation flight for drag reduction on the c-17 aircraft. In *AIAA Atmospheric Flight Mechanics Conference*, Minneapolis, MN, August 2012. AIAA.

[6] S. Andrew Ning, Tristan C. Flanzer, and Ilan M. Kroo. Aerodynamic performance of extended formation flight. *Journal of Aircraft*, 48(3):855–865, 2011.

[7] Stefan R. Bieniawski, Steven Rosenzweig, and William B. Blake. Summary of flight testing and results for the formation flight for aerodynamic benefit program. In *52nd Aerospace Sciences Meeting*, National Harbor, MD, January 2014. AIAA.

[8] Curt Hanson, Joe Pahle, James Reynolds, Andrade Stephanie, and Nelson Brown. Experimental measurements of fuel savings during aircraft wake surfing. In *Atmospheric Flight Mechanics Conference*, Atlanta, GA, January 2018. AIAA.

[9] S.A. Ning. *Aircraft drag reduction through extended formation flight*. PhD thesis, Stanford University, 2011.

[10] Robert Luckner. Modeling and simulation of wake vortex encounters: state-of-the-art and challenges. In *AIAA Modeling and Simulation Technologies (MST) Conference*, Minneapolis, MN, August 2012. AIAA.

[11] André Kaden and Robert Luckner. Modeling wake vortex roll-up and vortex-induced forces and moments for tight formation flight. In *AIAA Modeling and Simulation Technologies (MST) Conference*, Boston, MA, August 2013. AIAA.

[12] Karl Heinz Kienitz, André Kaden, and Robert Luckner. Modeling and design considerations for robust control of aircraft in tight cruise formation. In *AIAA Guidance, Navigation and Control (GNC) Conference*, Boston, MA, August 2013. AIAA.

[13] Michael A. Niestroy, Robert Luckner, Andre Koloschin, Nelson Brown, Curtis E. Hanson, and Carsten Doll. Flight control systems for aircraft engaged in air wake surfing for efficiency. In *AIAA Scitech 2020 Forum*, Orlando, FL, January 2020. AIAA.

[14] Daniel Barbuto Rossato and Karl Heinz Kienitz. Structured H_∞ synthesis: A systematic design approach for fully and underactuated systems. *Aerospace Science and Technology*, 119, 2021.

[15] R K. Nangia and Nelson Brown. Formation flying (air-wake-surfing) for efficient operations - NATO STO Research Task AVT-279. In *AIAA Scitech 2020 Forum*, Orlando, FL, January 2020. AIAA.

[16] Dietrich Hanke and Klaus-Uwe Hahn. In-flight simulator VFW 614 ATTAS. In Peter G. Hamel, editor, *In-Flight Simulators and Fly-by-Wire/Light Demonstrators*, chapter 9, pages 207–278. Springer International Publishing, Braunschweig, 2017.

[17] R.C. Nelson. *Flight stability and automatic control*. McGraw-Hill, New York, 3 edition, 1989.

[18] Sigurd Skogestad and Ian Postlethwaite. *Multivariable feedback control: analysis and design*. John Wiley & Sons, Hoboken, NJ, 2 edition, 2005.

[19] Vahram Stepanyan, Kalmanje Krishnakumar, and Nhan Nguyen. Adaptive control of a transport aircraft using differential thrust. In *AIAA Guidance, Navigation and Control (GNC) Conference*, Chicago, IL, August 2009. AIAA.

[20] Long K. Lu and Kamran Turkoglu. Adaptive differential thrust methodology for lateral/directional stability of an aircraft with a completely damaged vertical stabilizer. *International Journal of Aerospace Engineering*, 2018, 2018.